Two- and Three-dimensional properties of the Tri-Lab Verification Test Suite for Code Project A

Francis X. Timmes X-2
Bruce Fryxell X-2
George M. Hrbek X-1

Los Alamos National Laboratory
Los Alamos, NM 87545 USA

September 29, 2006

0. Contents   2

List of Figures

List of Tables

1. Summary

What's New:

- Two- and three dimensional verification analysis on uniform and adaptive meshes. Previous efforts considered only the Noh and Sedov test problems in 2D on uniform (Kamm & Kirkpatrick 2004) and adaptive (Timmes, Gisler & Hrbek 2005) meshes. The present analysis considers all the Tri-Lab problems in 2D and 3D, quantitatively assessing how well RAGE retains fidelity and symmetry to the underlying physics when motions and gradients are not necessarily grid-aligned.

- The Tri-Lab Verification Test suite has become part of the daily regression testing. Daily execution of script that generates the RAGE input decks, runs the code, compares the numerical and analytical solutions, performs the multi-dimensional verification analysis, and plots the key results has become part of Code Project A's daily regression testing (Hrbek et al., 2005; Ankeny & Brock 2006).

- New analytic solution for the two-dimensional cell-averaged solution of the Coggeshall #8 problem (Timmes & Clover 2006). The solution reduces the global error norm by an order of magnitude in numerical solutions done with RAGE.

- New initialization module for Reinicke Meyer-ter-Vehn problem permits this test problem to be performed in 2D and 3D for the first time. The new module also provides a more accurate and smoother initial state, which is of particular importance for convergence studies on adaptive meshes.

- LLNL's B-division verification efforts on the Tri-Lab Verification Test Suite is using 4 of our analytic solution codes (Frank Graziani, Carole Woodward).

- Archiving analytic solution codes, input decks, and results on SourceForge. Building on previous efforts often required knowing who to ask for what. All relevant material is now stored in a centralized repository.

Results:

- In general, RAGE shows a high degree of symmetry and fidelity to the underlying physics for test problems in slab geometries. All of the test problems run in axisymmetric geometries have problems with either large asymmetries or outright anomalies, particularly for locations near the z-axis. The Cog-8 problem has large errors for locations near the z-axis, the RMTV problem shows larger errors on adaptive grids than on the corresponding uniform grids, the Noh problem has a disastrous low density bubble near the z-axis on adaptive meshes, and the shock fails to reach the correct location along the z-axis for the Sedov problem because of a high pressure bubble.

- The computational efficiency of using adaptive grids instead of uniform grids is typically about a factor of twenty for 4-6 levels of mesh refinement for 2D versions of problems in the Tri-Lab Test Suite. This efficiency gain isn't generally accompanied by a corresponding reduction in the error between the numerical and analytical solutions for the same effective spatial resolution when the default AMR settings are used. For several Tri-Lab test problems the relative errors on adaptive grids are larger than the errors on corresponding uniform grids.

Recommended Directions:

- Develop and implement better AMR packages for Code Project A. Tremendous resources have gone into developing the physics modules, but not the grid technology on which that physics is computed. There doesn't appear to be a single team directly associated with Code Project A examining present and next-generation AMR technology - this represents a growth opportunity.

- Replace the Mader HE detonation test problem. The parameters of Forest-Fire model are cell size and equation of state dependent, which presents serious difficulties for performing verification studies on different meshes. If the purpose of this test problem in the Tri-Lab Verification Test Suite is to verify detonation wave physics, then there are several detonation problems which have far less idiosyncrasies. If the purpose of the test problem is to verify HE burn models, then additional plans are needed since NOBEL is essentially an unsupported product that hasn't been updated since 2005.

- Continue developing and applying rigorous calculation verification procedures for 2D problems that don't admit an exact solution (Smitherman, Kamm & Brock 2005; Tippett & Timmes 2006). This is a key growth direction for verification efforts to bridge the gap between analytical test problems and highly-complex applications.

- This report on multi-dimensional versions of the Tri-Lab Verification Test Suite and its companion report on 1D spatial-temporal convergence properties (Timmes, Fryxell & Hrbek) represent a certain closure to research efforts on Tri-Lab Verification Test Suite as it is presently defined (see Figure 1). New problems that exercise multi-material and/or multi-temperature solutions in an extension of the Tri-Lab Verification Test Suite will be discussed with Livermore and Sandia representatives at NECDC|06.

Analysis Coverage of the present Tri-Lab Verifcation Test Suite:

	1D uniform	1D AMR	1D temporal	1D scripted	2D uniform	2D AMR	2D scripted	3D uniform	3D AMR	3D scripted
Su & Olson	● (K&K)	● (TGH)	● (TGH)	● (TGH)	● (TGH)	● (TGH)	● (TGH)	● (TGH)	● (TGH)	● (TGH)
Cog8	● (K&K)	● (TGH)	● (TFH)	● (TGH)	● (TFH)	● (TFH)	● (TFH)	● (TFH)	● (TFH)	● (TFH)
Mader	● (K&K)	● (TGH)	● (TGH)	● (TGH)	● (TGH)	● (TGH)	● (TGH)	● (TGH)	● (TGH)	● (TGH)
RMTV	● (TGH)	● (TGH)	● (TFH)	● (TGH)	● (TFH)	● (TFH)	● (TFH)	● (TFH)	● (TFH)	● (TFH)
Noh	● (K&K)	● (TGH)	● (TFH)	● (TGH)	● (K&K)	● (TFH)	● (TFH)	● (TFH)	● (TFH)	● (TFH)
Sedov	● (K&K)	● (TGH)	● (TFH)	● (TGH)	● (K&K)	● (TFH)	● (TFH)	● (TFH)	● (TFH)	● (TFH)
Sood	● (K&K)	● (TGH)	● (TGH)	● (TGH)	● (TFH)	● (TFH)	● (TFH)			

Legend:
- ● (K&K) — Kamm & Kirkpatrick 2004
- ● (TGH) — Timmes, Gisler, & Hrbek 2005
- ● (TFH) — Timmes, Fryxell & Hrbek 2006

Figure 1. - Status of LANL's efforts on the Tri-Lab Verification Test Suite. Pioneering efforts by Kamm & Kirkpatrick (2004) supplied verification analyses on most of the problems on 1D uniform grids and for two problems on 2D uniform grids. Timmes, Gisler & Hrbek (2005) automated the verification process, extended coverage to adaptive meshes, initiated temporal domain verification, and ran additional problems in 2D and 3D. The present effort establishes spatial-temporal convergence and multi-dimensional versions of all the problems on uniform and adaptive meshes.

2. Tri-Lab Verification Test Suite

Most modern, complex simulations are done in two and three dimensions. It is important to consider how well hydrocodes duplicate the physics in situations where motions and gradients are not grid-aligned. Many complex simulations that use an Eulerian approach also employ adaptive mesh refinement (AMR). It is important to know if the fundamental assertion of AMR, that solutions on adaptive grids are as accurate as the solutions on corresponding uniform grids, is fulfilled for multi-dimensional versions of the Tri-Lab Verification Test Suite. Previous efforts considered only the Noh and Sedov problems in 2D on uniform (Kamm & Kirkpatrick 2004) and adaptive (Timmes, Gisler & Hrbek 2005) meshes. This report focuses on multi-dimensional versions of all the Tri-Lab Test problems on both uniform and adaptive meshes using programs from Code Project A.

The Tri-Lab verification test suite is presently defined by seven problems that have analytical solutions: Su & Olson, Mader, Reinicke Meyer-ter-Vehn, Coggeshall #8, Noh, Sedov, and Sood (Kamm & Kirkpatrick 2004; Figure 1). In this report RAGE 20060331.0240, was run on the Linux cluster Flash to generate numerical solutions on 2D and 3D uniform and adaptive meshes for all the Tri-Lab problems (NOBEL 20050331.021 was used for the Mader problem). The RAGE input decks used are the same ones archived by Timmes, Fryxell & Hrbek (2006), although several of the input decks were generalized to include temporal or multi-dimensional capability.

After the problems were run, John Grove's AMHCTOOLS (2005a, 2005b) was used to extract the solution data on the native grid from the binary dump files. If one requests the simulation data from RAGE, the data on the native mesh is interpolated onto uniform mesh. Extracting the solution data on the native mesh is important for proper verification analysis, particularly on adaptive meshes.

After the numerical solution on the native was extracted, the absolute L_1 norm and absolute L_2 norm were computed (Kamm, Rider & Brock 2002) as

$$L_{1,\mathrm{abs}} = \frac{\sum(f_i^{\mathrm{exact}} - f_i^{\mathrm{rage}})V_i}{\sum V_i} \qquad\qquad L_{2,\mathrm{abs}} = \left[\frac{\sum(f_i^{\mathrm{exact}} - f_i^{\mathrm{rage}})^2 V_i}{\sum V_i}\right]^{1/2} \qquad (1)$$

where V_i is the appropriate volume element weighting. To be specific, two-dimensional versions of the Su-Olson, Mader, and Sood problems run in slab geometry have $V_i = \Delta x_i \Delta y_i$ where Δx_i is the grid spacing in the x-direction and Δy_i is the grid spacing in the y-direction. Since RAGE enforces square cells, $\Delta x_i = \Delta y_i$. Two-dimensional versions of the spherical Reinicke Meyer-ter-Vehn, Coggeshall #8, Noh, and Sedov problems run in axisymmetric coordinates have volume $V_i = 2\pi\Delta r\Delta z$. In this manner the norm weights correspond to how the variable of interest is treated in the solver, e.g., volume averaged variables have volume norm weights.

After the global error norms were computed, the rates of convergence were determined. For cases where the time-step controller was held constant and the spatial resolution varied, the $L_{1,\mathrm{abs}}$ error norm was assumed to obey

$$L_{1,\mathrm{abs}} = A\left(\Delta x\right)^{\alpha} \;\;, \qquad (2)$$

where Δx is the cell spacing and α is the spatial convergence rate (Kamm, Rider & Brock 2002). In this case the rate of convergence between two grids, one coarse and one fine, is given explicitly by

$$\alpha = \log\left[\frac{L_{1,\mathrm{abs,fine}}}{L_{1,\mathrm{abs,coarse}}}\right] \Big/ \log\left[\frac{\Delta x_{\mathrm{fine}}}{\Delta x_{\mathrm{coarse}}}\right] \;\;. \qquad (3)$$

This error model follows from a modified-equation analysis which is typically done in terms of length scales - not volumes. That is, while some problems may use volume elements to compute an error norm, the error model always uses grid spacings. This raises a pragmatic issue, particularly for problems run with adaptive mesh refinement. The RAGE dump files, which are cracked by AMHCTOOLS, reports the cell's volume. For 2D Cartesian coordinates the volume reported is easily converted to the mesh spacing Δx. For 2D axisymmetric geometries the volume reported is the shell volume of a right circular torus, which is suitable for the error norm calculation, but we need Δr for the convergence calculations. While RAGE/AMHCTOOLS reports the cell center r, it doesn't directly report either the mesh spacing Δr or the inner and outer radii of the spherical shell. We derived the radial mesh spacing as follows. The shell volume is

$$V = \pi \Delta z \left(r_{\text{outer}}^2 - r_{\text{inner}}^2 \right) = \pi \Delta z \left[\left(r + \frac{\Delta r}{2} \right)^2 - \left(r - \frac{\Delta r}{2} \right)^2 \right] \quad . \tag{4}$$

Since RAGE enforces square cells, $\Delta z = \Delta r$, the solution for the radial grid spacing reduces to a simple quadratic whose solution is

$$\Delta r = \sqrt{\frac{V}{2\pi r}} \tag{5}$$

Equations (4) and (5) are valid on both uniform and adaptive meshes in RAGE.

For cases where the spatial resolution was held constant and the temporal resolution varied, the global error norms were assumed to obey

$$L_{1,\text{abs}} = B \left(\Delta t \right)^{\beta} \tag{6}$$

where Δt is the cell spacing and β is the temporal convergence rate. In this case the rate of convergence between two temporal resolutions, one coarse and one fine, is given explicitly by

$$\beta = \log \left[\frac{L_{1,\text{abs,fine}}}{L_{1,\text{abs,coarse}}} \right] \bigg/ \log \left[\frac{\Delta t_{\text{fine}}}{\Delta t_{\text{coarse}}} \right] \quad . \tag{7}$$

One-dimensional cases where both the time-step and spatial resolution were varied are discussed in Timmes, Fryxell, & Hrbek (2006).

It should be noted that the spatial discretization errors, temporal discretization errors, or coupled space-time errors may change with time during the numerical simulation. As various physical effects are exercised in different proportions during an evolution, the dominant contributor to the overall numerical error may not remain the same (Hemez 2005). For example, the effects of time discretization on a hydrodynamic simulation may be more pronounced early in the evolution. Likewise, inadequate spatial discretization at some instants of the simulation may be replaced as the dominant source of solution error by truncation errors at other times (Hemez 2005). These remarks imply that convergence coefficients in equation may be functions of spacetime. To keep the present study practical, we consider only the code verification properties at the ending time of a test problem's evolution.

The foregoing analysis has become part of the daily regression testing. That is, daily execution of script generates the RAGE input decks, runs the code, compares the numerical and analytical solutions, performs the spatial-temporal verification analysis, and plots the key results (Hrbek et al., 2005; Ankeny & Brock 2006).

The remainder of this report details the verification analysis of the Tri-Lab Verification Test Suite, focusing on the symmetries present in two- and three-dimensional simulations.

2.1 The Su & Olson Problem

The Su & Olson problem is a one-dimensional, half-space, non-equilibrium Marshak wave problem. There is no hydrodynamics in this test problem. The radiative transfer model is a one-group diffusion approximation with a finite radiation source boundary condition, where the radiative and material fields are out of equilibrium. As the energy density of the radiation field increases, energy is transfered to the material (see Figure 2). Su & Olson (1996) found a quadrature solution for the distribution of radiative energy and material temperature as a function of spacetime. This test problem is useful for verifying time-dependent radiation diffusion codes. A succinct description of the Su & Olson problem for the Tri-Lab Verification Test Suite, fortran code for generating solutions, and the 1D spatial-temporal convergence properties are given in Timmes, Gisler & Hrbek (2005) and Timmes, Fryxell & Hrbek (2006).
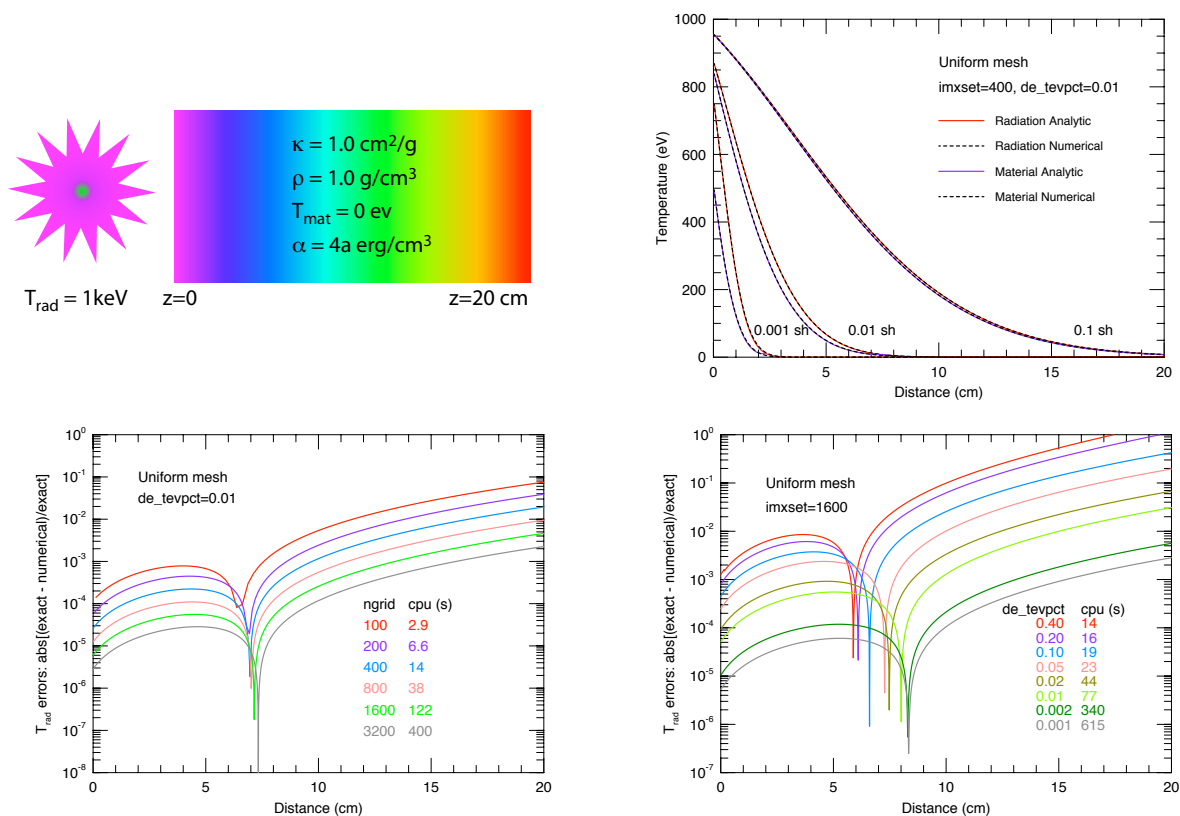
Figure 2. - Summary of the Su & Olson problem in 1D. Shown are the basic setup (upper left), numerical and analytical solutions at 0.1 sh (upper right), relative errors in the radiation temperature for a uniform grid at a fixed time-step (lower left), and the relative error in the radiation temperature for various time-step control values on a fixed uniform grid.

Figure 2 expresses a summary of the one-dimensional version of the Su & Olson problem. The setup and parameters are illustrated in the upper left. A representative solution on a uniform mesh of 400 cells at 0.001, 0.01 and 0.1 sh is shown in the upper right. Initially, the radiation streams into the slab and the material temperature lags behind the radiation temperature. As the radiation energy density builds up, the material temperature catches up, and

by t=0.1 sh the radiation and material temperatures are essentially identical.

In the lower left of Figure 2 is the absolute value of the relative errors in the radiation temperature on uniform grids with 100, 200, 400, 800, 1600, and 3200 cells at the final time of 0.1 sh. Cusps are due to changes of sign in the relative error, and the relative cpu cost on a single processor of increasing the spatial resolution is given. The parameter de_tevpctd sets the maximum relative change in the radiation temperature allowed per time-step, and is used to determine the time-step in the numerical solution of the Su & Olson problem. It was set at a relatively strict value of 0.01, limiting changes in the radiation temperature to a maximum of 1% in a time-step. The radiation temperature is in the spatial asymptotic regime with a roughly linear convergence rate at this time-step control setting. In the lower right of Figure 2 is the absolute value of the relative errors in the radiation temperature for time-step controller values of de_tevpct=0.4, 0.2, 0.1, 0.05, 0.02, 0.01, 0.0002, 0.001 on a uniform grid of 1600 cells at the final time of 0.1 sh. The radiation temperature is in the temporal asymptotic regime with a roughly linear convergence rate at this spatial resolution.

The default criteria for triggering adaptive mesh refinement, gradients in the pressure or mass density, don't produce much refinement for this hydrodynamics-free Marshak wave problem (Timmes, Gisler & Hrbek 2005). As a result, the solution and errors on 1D adaptive meshes is quantitatively very similar to the numbers for uniform grids.

The left column of Figure 3 shows the radiation temperature for the Su & Olson problem on 100x100, 200x200, 400x400, and 800x800 uniform grids at the final time of 0.1 sh. Even at this coarse visual level, the intrinsic 1D nature of the test problem is apparent; at any y-coordinate the temperature is commensurate with the values indicated by Figure 2. In the middle column of Figure 3 is the absolute value of the radiation temperature's error relative error to the analytic solution on the same grids at the same ending time. The cusps at $x \sim 7$ cm are due to changes of sign in the relative error, and the magnitude of the errors are almost exactly the same as given by Figure 2. As a result, a verification analysis on the 2D simulations yields the spatial-temporal convergence rates that are the same (to within 5 significant figures) as their 1D counterparts. In the right column of Figure 3 is the asymmetry of the numerical solutions on the same grids at the same ending time. For any value of the x-coordinate, the y-averaged value of the radiation temperature was determined. The color maps then reveal the relative difference between the radiation temperature and the y-averaged radiation temperature. Such plots essentially expose the deviations from slab symmetry. The amplitude of these deviations is always less than 10^{-8}. In other words, RAGE is performing admirably in keeping this 1D problem essentially 1D.

Figure 4 is the adaptive mesh counterpart of Figure 3 for the material temperature. The dots in the figure represent the grid pints where the various solutions were computed, the color of the dot indicative of the magnitude of the radiation field. White areas indicate regions where there is no grid, and heavily refined areas appear as continuous color maps. The left column of Figure 4 shows the material temperature for a Su & Olson problem on adaptive grids with effective resolutions (if maximally refined everywhere) of 100x100, 200x200, 400x400, and 800x800 cells at the final time of 0.1 sh. The base grid was a uniform 100x100 mesh. The middle column of Figure 4 displays the relative errors in the material temperature, while the right column reveals the asymmetries in the numerical solution. Figure 4 reveals that the default criteria for refining a mesh don't produce much refinement for the Su & Olson problem. As a result, the solution and relative errors on 2D adaptive meshes is largely the same as for the base 100x100 uniform grid. Note the heavy grid refinement and larger errors near $x \sim 18$ cm in the adaptive mesh solutions. This feature
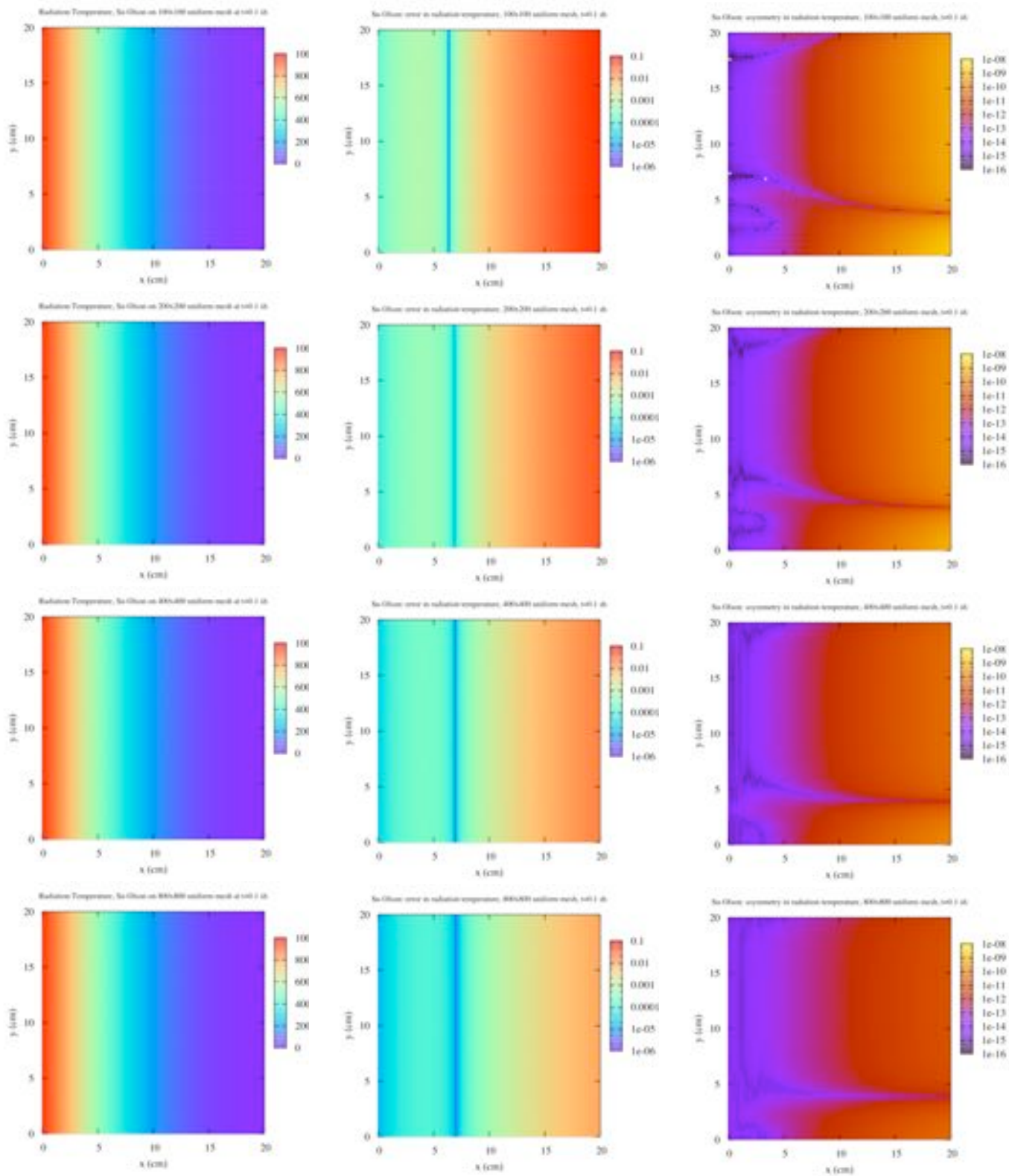
Figure 3. - Radiation temperature (left), relative errors (middle), and asymmetries (right) for the Su& Olson problem on 100x100, 200x200, 400x400, and 800x800 uniform grid at t=0.1 sh.
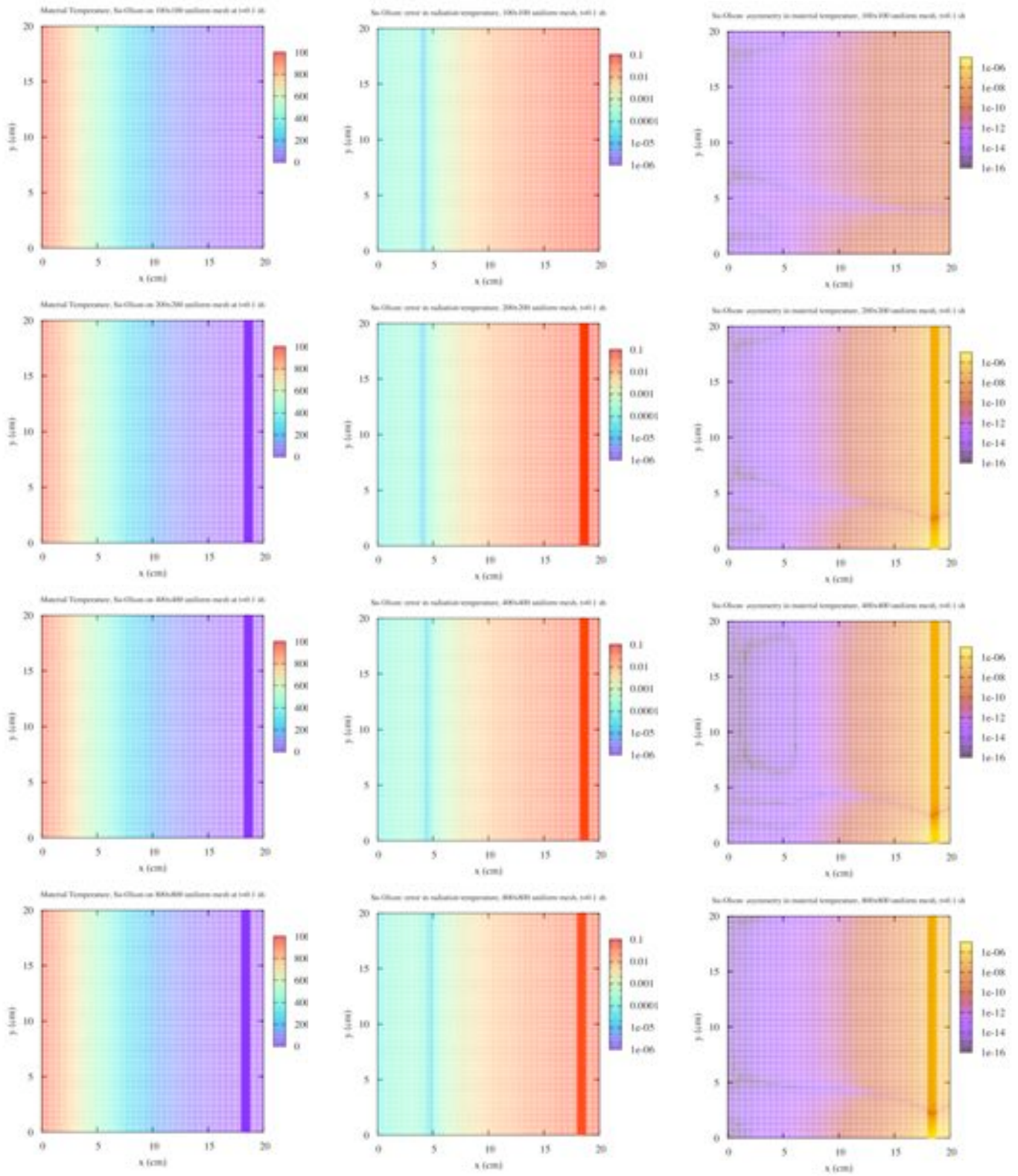
Figure 4. - Material temperature (left), relative errors (middle), and asymmetries (right) for the Su & Olson problem on 100x100, 200x200, 400x400, and 800x800 adaptive grids at t=0.1 sh.

appears to be seeded very early ($t \leq 10^{-11}$ s) in the evolution. The nature and removal of this feature should be investigated in a follow-up report.

Table 1 details the convergence properties for the Su & Olson problem on 2D uniform grids, and Table 2 shows the same information for adaptive grids. For uniform grids, the radiation and material temperatures is in the spatial asymptotic regime with a roughly linear convergence rate at this time-step control setting. For adaptive grids, the convergence rate is considerably less ($\alpha \sim 0.2$), because the default mesh refinement criteria doesn't trigger much refinement for the Su & Olson problem. As a result, the L_1 error norm on 2D adaptive meshes is largely the same as for the base 100x100 uniform mesh.

Table 1
Spatial Convergence Coefficients for the Su & Olson Problem on 2D Uniform Grids

| # of cells | T_{rad} | | | T_{mat} | | |
	$L_{1,abs}$	α	A	$L_{1,abs}$	α	A
100x100	6.804E-01			8.583E-01		
200x200	3.364E-01	1.016E+00	7.338E+01	4.778E-01	8.451E-01	4.206E+01
400x400	1.666E-01	1.014E+00	7.229E+01	2.452E-01	9.625E-01	7.834E+01
800x800	8.204E-02	1.022E+00	7.608E+01	1.241E-01	9.824E-01	8.825E+01

Table 2
Spatial Convergence Coefficients for the Su & Olson Problem on 2D Adaptive Grids

| maximum # of cells | actual # of cells | T_{rad} | | | T_{mat} | | |
		$L_{1,abs}$	α	A	$L_{1,abs}$	α	A
100x100	10000	6.486E-01			7.800E-01		
200x200	11200	6.315E-01	3.841E-02	7.741E-01	7.613E-01	3.508E-02	9.168E-01
400x400	13600	5.499E-01	1.996E-01	1.818E+00	6.233E-01	2.885E-01	3.510E+00
800x800	14800	4.932E-01	1.570E-01	1.409E+00	5.344E-01	2.221E-01	2.359E+00

Figure 5 shows the radiation temperature for a 3D Su & Olson problem on adaptive grid with an effective resolution, if maximally refined, of 100x100x100 at the final time of 0.1 sh. The base grid was a uniform 50x50x50 mesh. As in the 2D case, RAGE did an excellent job of maintaining the 1D symmetry of the problem. One difficulty we faced in the analysis of the 3D versions of the Tri-Lab Test problems was our inability to find a suitable visualization tool - a tool not just for the RAGE dump files, but for an arbitrary verification or asymmetry analysis. Of course, one could always take slices through planes parallel to the coordinate axes to reduce the analysis to 2D. For the Su & Olson problem this gives results that are quite consistent with the results presented above.
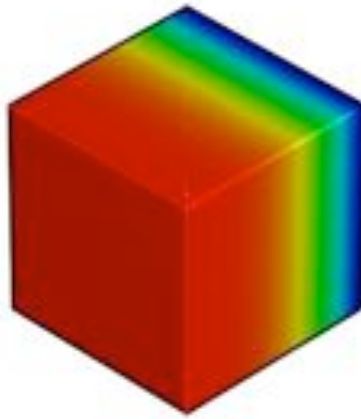
Figure 5. - Material temperature for a 3D Su & Olson problem on a 100x100x100 adaptive mesh at t=0.1 sh.

2.2 The Coggeshall #8 Problem

Coggeshall (1991) published a collection of analytic self-similar test problems, and ``Coggeshall #8'' or ``Cog8'' is the eighth one listed. The solution to this problem represents an adiabatic expansion plus heat conduction (see Figure 6). The heat conduction's area weighted flux on each cell face is equal. That is, conduction moves as much energy into a cell as it removes. Thus, the answers with and without conduction look much the same (Clover 2006). A succinct description of the Cog8 problem for the Tri-Lab Verification Test Suite, fortran code for generating solutions, and the 1D spatial-temporal convergence properties are discussed in Timmes, Gisler & Hrbek (2005) and Timmes, Fryxell & Hrbek (2006).

Figure 6 shows a summary of the one-dimensional version of the Cog8 problem. The setup and parameters are illustrated in the upper left. A representative solution on a uniform mesh of 200 cells with a time-step controller of tstab=0.2 is shown in the upper right at the final time of t=20 sh. Analytical and numerical solutions are overlayed for the mass density, velocity, pressure, and temperature.
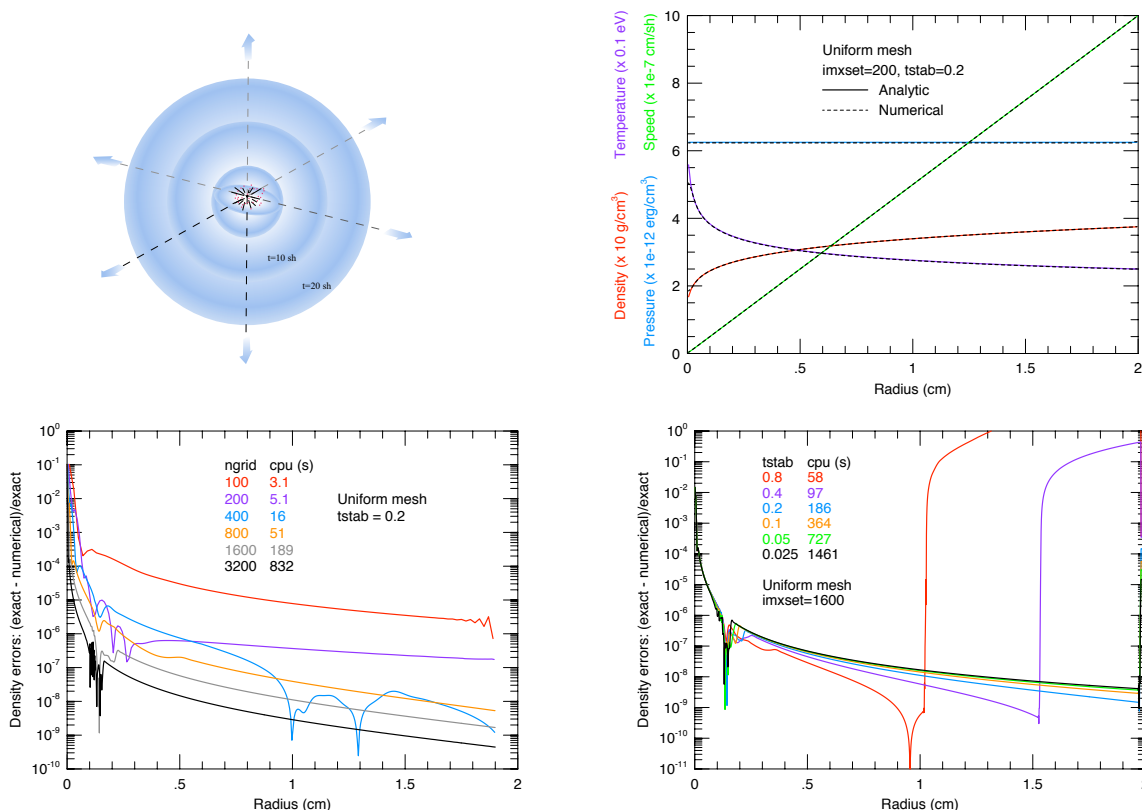
Figure 6. - Summary of the Cog8 problem in 1D. Shown are the basic setup (upper left), numerical and analytical solutions (upper right), relative errors in the density for a variety of uniform grids at a fixed time-step (lower left), and the relative error in the density for a variety of time-step control values on a fixed uniform grids.

The image in the lower left of Figure 6 depicts the absolute value of the relative errors in the cell-averaged density for a variety of uniform grids at the ending time of t=20 sh. The parameter tstab sets change in the time step allowed

by the material speed, $\Delta t = $ tstab $\cdot \Delta x / (|v_x| + |v_y| + |v_z|)$, and determines the time-step in the numerical solution of the Cog8 problem. It was set to its default value of 0.2, limiting transport of material to 20% of a cell's width. Cusps are due to changes of sign in the relative error, and the relative cpu cost on a single processor of increasing the spatial resolution is given. In general, the error decreases with increasing resolution. However, there are large, persistent errors at the inner boundary. Getting the right amount of energy to flow into an origin of a sphere is an unsolved problem, so an error accumulates at the origin whether using the point-wise or cell-averaged quantities. The pressure and temperature (neither shown) have linear convergence rates while the density and material speed (not shown) have nearly quadratic convergence rate with spatial resolution at this time-step control setting.

The image in the lower right of Figure 6 displays the absolute value of the relative errors in the density for a variety of time-step control values on a uniform grid of 1600 cells. Cusps are due to changes of sign in the relative error, and the relative cpu cost on a single processor of increasing the temporal resolution is given. Values of tstab ≥ 0.4 produce inaccurate results near the right boundary at the beginning of the simulation, and that error propagates inwards into the domain. For these large values of tstab, the Cog #8 test problem violates the recommended accuracy criteria of the code. Neglecting the large values of the time-step controller, the density has a convergence rate $\beta \sim 0$ at 1600 cells and the smallest values of tstab. Although not shown, the pressure has $\beta \sim 1$, the temperature about $\beta \sim 0.2$, and the material speed about $\beta \sim 0.8$.

A new analytic solution for the two-dimensional cell-averaged solution of the Cog8 problem is given by Timmes & Clover (2006). Briefly, we considered a generalized density evolution for the Cog8 problem of the form $\rho = \rho_0 \, r^{\mathrm{rp}}/t^{\mathrm{tp}}$, where ρ_0 is the initial density. Excluding boundary points, they found the cell-averaged solution for the mass enclosed by a cell in axisymmetric geometry is

$$M(r,z,t) = \frac{2\pi\rho_0}{t^{\mathrm{tp}}(2+\mathrm{rp})}\left[z_u r_u^{2+\mathrm{rp}} \, {}_2F_1\left(\frac{1}{2}, -\frac{2+\mathrm{rp}}{2}, \frac{3}{2}, -\frac{z_u^2}{r_u^2}\right) \; - \; z_u r_l^{2+\mathrm{rp}} \, {}_2F_1\left(\frac{1}{2}, -\frac{2+\mathrm{rp}}{2}, \frac{3}{2}, -\frac{z_u^2}{r_l^2}\right) \right.$$

$$\left. -z_l r_u^{2+\mathrm{rp}} \, {}_2F_1\left(\frac{1}{2}, -\frac{2+\mathrm{rp}}{2}, \frac{3}{2}, -\frac{z_l^2}{r_u^2}\right) \; + \; z_u r_l^{2+\mathrm{rp}} \, {}_2F_1\left(\frac{1}{2}, -\frac{2+\mathrm{rp}}{2}, \frac{3}{2}, -\frac{z_l^2}{r_l^2}\right) \right] \; , \qquad (8)$$

where ${}_2F_1(a,b,c,w)$ is a hypergeometric function. The upper (subscript u) and lower (subscript l) limits of a cell are r_l, r_u, z_l, and z_u. Special forms of equation (8) apply at the points where boundary conditions apply. The cell-averaged momentum is

$$p(r,z,t) = \frac{2\pi\rho_0}{t^{1+\mathrm{tp}}(3+\mathrm{rp})}\left[z_u r_u^{3+\mathrm{rp}} \, {}_2F_1\left(\frac{1}{2}, -\frac{3+\mathrm{rp}}{2}, \frac{3}{2}, -\frac{z_u^2}{r_u^2}\right) \; - \; z_u r_l^{3+\mathrm{rp}} \, {}_2F_1\left(\frac{1}{2}, -\frac{3+\mathrm{rp}}{2}, \frac{3}{2}, -\frac{z_u^2}{r_l^2}\right) \right.$$

$$\left. -z_l r_u^{3+\mathrm{rp}} \, {}_2F_1\left(\frac{1}{2}, -\frac{3+\mathrm{rp}}{2}, \frac{3}{2}, -\frac{z_l^2}{r_u^2}\right) \; + \; z_u r_l^{3+\mathrm{rp}} \, {}_2F_1\left(\frac{1}{2}, -\frac{3+\mathrm{rp}}{2}, \frac{3}{2}, -\frac{z_l^2}{r_l^2}\right) \right] \; , \qquad (9)$$

and the cell-averaged kinetic energy is

$$KE(r,z,t) = \frac{\pi\rho_0}{t^{2+\mathrm{tp}}(4+\mathrm{rp})}\left[z_u r_u^{4+\mathrm{rp}} \, {}_2F_1\left(\frac{1}{2}, -\frac{4+\mathrm{rp}}{2}, \frac{3}{2}, -\frac{z_u^2}{r_u^2}\right) \; - \; z_u r_l^{4+\mathrm{rp}} \, {}_2F_1\left(\frac{1}{2}, -\frac{4+\mathrm{rp}}{2}, \frac{3}{2}, -\frac{z_u^2}{r_l^2}\right) \right.$$

$$\left. - z_l r_u^{4+\mathrm{rp}} \, {}_2F_1\left(\frac{1}{2}, -\frac{4+\mathrm{rp}}{2}, \frac{3}{2}, -\frac{z_l^2}{r_u^2}\right) \; + \; z_u r_l^{4+\mathrm{rp}} \, {}_2F_1\left(\frac{1}{2}, -\frac{4+\mathrm{rp}}{2}, \frac{3}{2}, -\frac{z_l^2}{r_l^2}\right) \right] \; . \qquad (10)$$

In the Cog8 problem the temperature follows an evolution that is different than the density, but still a power-law. For a temperature evolution of $T = T_0 \, r^{\mathrm{b}}/t^{\mathrm{c}}$, they found the cell-averaged temperature as

$$T(r,z,t) = \frac{2\pi T_0}{t^{\mathrm{c}}(2+\mathrm{b})} \left[z_u r_u^{2+\mathrm{b}} \, {}_2F_1\left(\frac{1}{2}, -\frac{2+\mathrm{b}}{2}, \frac{3}{2}, -\frac{z_u^2}{r_u^2}\right) - z_u r_l^{2+\mathrm{b}} \, {}_2F_1\left(\frac{1}{2}, -\frac{2+\mathrm{b}}{2}, \frac{3}{2}, -\frac{z_u^2}{r_l^2}\right) \right.$$

$$\left. - z_l r_u^{2+\mathrm{b}} \, {}_2F_1\left(\frac{1}{2}, -\frac{2+\mathrm{b}}{2}, \frac{3}{2}, -\frac{z_l^2}{r_u^2}\right) + z_u r_l^{2+\mathrm{b}} \, {}_2F_1\left(\frac{1}{2}, -\frac{2+\mathrm{b}}{2}, \frac{3}{2}, -\frac{z_l^2}{r_l^2}\right) \right] \quad . \qquad (11)$$

Their improved two-dimensional cell-averaged solution for the Cog8 test problem has been implemented in RAGE's test problem modules. Some of the differences between point-wise and cell-averaged solutions will be discussed below; a full comparison is given in Timmes & Clover (2006).
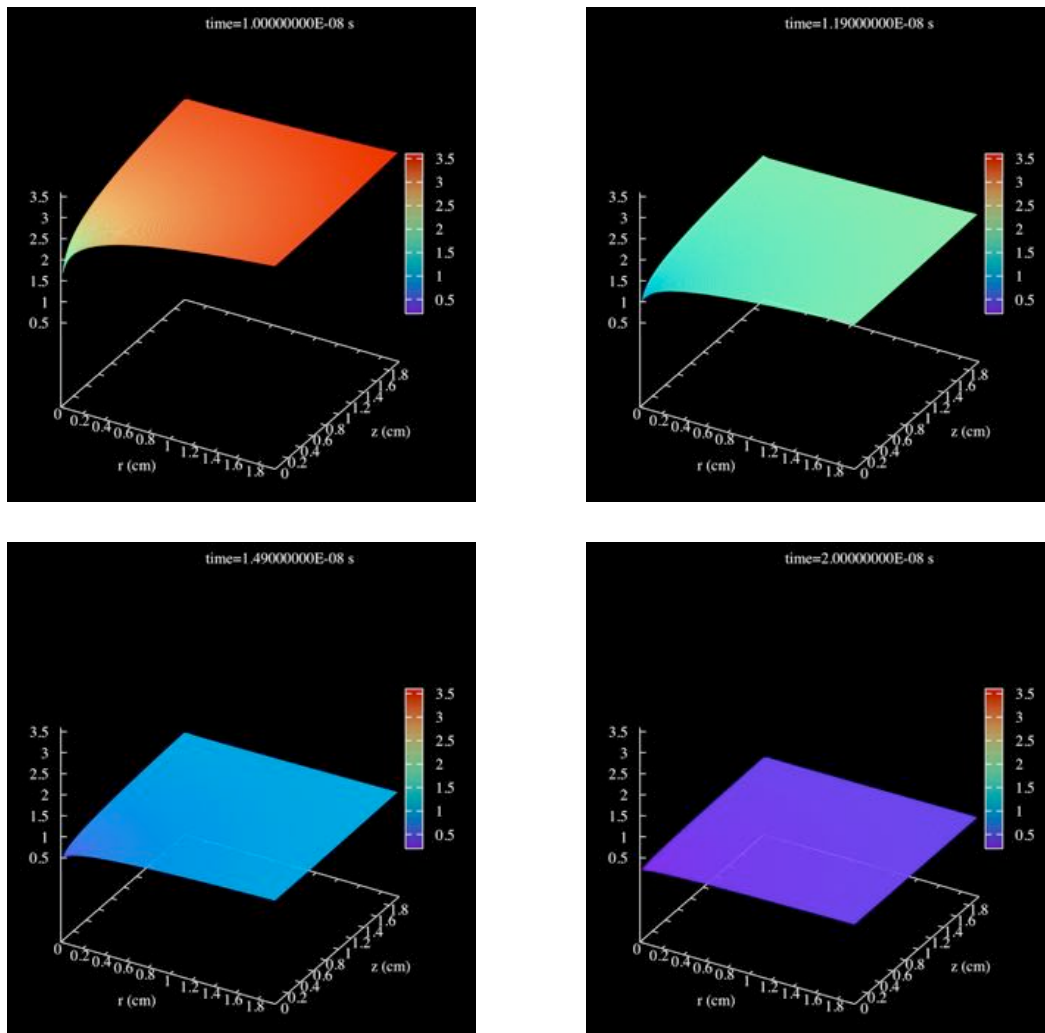

Figure 7. - Frames from a movie of the density evolution on a 100x100 uniform grid with a time-step control value of tstab=0.2.

Figure 7 exhibits four frames from a movie of the density for the Cog8 problem on a 100x100 uniform mesh. As the material expands, via $v = r/t$, the density drops quicker farther from the origin. At this visual level of comparison, the intrinsic spherically symmetric nature of the test problem may not be apparent, but at any value of the radial distance from the origin the density is commensurate with the values indicated by Figure 6.

Figure 8 compares the absolute value of the relative errors in the density field when the solution is initialized with the point-wise solution and cell-averaged solution. The left column of images shows the relative errors for the point-wise approach on uniform grids of 100x100, 200x200, 400x400, and 800x800. The right column displays the relative errors for the cell-averaged approach on the same set of grids. In all cases the time step was determined by tstab=0.2. White areas indicate cusps, where the relative error changes sign. Both the point-wise and cell-averaged approaches have their largest relative errors near the z-axis, indicating the numerical solution is generating an asymmetric solution. The point-wise error fields exhibit a strong symmetry along the diagonal with two distinct cusps on either side of the diagonal. The cell-averaged error field is smoother, has a smaller error, and also possesses a symmetry along the diagonal, although not as prominent.

Table 3 details the convergence properties for the Cog #8 problem on 2D pointwise grids, and Table 4 specifies the same information for cell-averaged grids. For uniform grids with point-wise analytic solutions, the density, pressure, temperature, and material speed are in the spatial asymptotic regime with roughly linear convergence rates at this time-step control setting. For the cell-averaged solutions on uniform grids, the convergence rates and magnitudes of the L_1 error norms are similar. In both cases the error is dominated by a strip near the z-axis. So, while the cell-averaged solution in 1D produces significantly smaller errors and similar convergence rates, the cell-averaged solution in 2D produces similar relative errors and convergence rates, although the relative error field is smoother.

Table 3

Spatial Convergence Coefficients for the Coggeshall #8 Problem on 2D uniform Grids for Point-wise Analytic Solutions

	Density			Pressure		
# of cells	$L_{1,abs}$	α	A	$L_{1,abs}$	α	A
100x100	2.308E-04			9.577E+09		
200x200	5.473E-05	2.076E+00	3.281E+00	3.306E+09	1.534E+00	1.121E+13
400x400	1.376E-05	1.992E+00	2.093E+00	1.289E+09	1.359E+00	4.437E+12
800x800	3.507E-06	1.972E+00	1.866E+00	5.711E+08	1.174E+00	1.464E+12
	Temperature			Speed		
# of cells	$L_{1,abs}$	α	A	$L_{1,abs}$	α	A
100x100	2.667E-02			1.796E+03		
200x200	1.055E-02	1.338E+00	1.267E+01	4.623E+02	1.958E+00	1.481E+07
400x400	4.678E-03	1.173E+00	5.278E+00	1.241E+02	1.897E+00	1.074E+07
800x800	2.348E-03	9.947E-01	1.812E+00	3.266E+01	1.926E+00	1.273E+07

Table 4

Spatial Convergence Coefficients for the Coggeshall #8 Problem on 2D uniform Grids for Cell-Averaged Analytic Solutions

	Density			Pressure		
# of cells	$L_{1,abs}$	α	A	$L_{1,abs}$	α	A
100x100	2.490E-04			1.024E+10		
200x200	5.911E-05	2.074E+00	3.508E+00	3.522E+09	1.540E+00	1.230E+13
400x400	1.507E-05	1.972E+00	2.037E+00	1.371E+09	1.361E+00	4.768E+12
800x800	5.923E-06	1.347E+00	4.821E-02	6.004E+08	1.192E+00	1.729E+12
	Temperature			Speed		
# of cells	$L_{1,abs}$	α	A	$L_{1,abs}$	α	A
100x100	2.792E-02			1.839E+03		
200x200	1.106E-02	1.336E+00	1.315E+01	4.329E+02	2.087E+00	2.746E+07
400x400	4.921E-03	1.168E+00	5.383E+00	1.060E+02	2.029E+00	2.023E+07
800x800	2.590E-03	9.263E-01	1.266E+00	1.817E+02	-7.768E-01	1.010E+00

The asymmetries in the numerical solutions on uniform grids are revealed in Figure 9. Across any row is the asymmetry in the mass density, temperature and material speed. Down any column are the asymmetries on 100x100, 200x200, 400x400, and 800x800 uniform grids at the ending time t=20 sh. The color maps plot the relative difference between the field and its radially-averaged value. These plots essentially give the deviations from spherical symmetry. Note that the amplitude of these deviations is generally between 10^{-2} and 10^{-6}, suggesting that RAGE is keeping a spherically symmetric problem reasonably symmetric. The density, pressure, and material speed all have their largest relative asymmetries near the z-axis.

Asymmetries in the numerical solution for the density on adaptive grids are shown in Figure 10. The adaptive grids have effective resolutions (if maximally refined everywhere) of 100x100, 200x200, 400x400, and 800x800 cells. The base grid was a uniform 100x100 grid. As in Figure 9, the color maps plot the relative difference between the density and its radially-averaged value, and reveal the asymmetry of the numerical solution. Figure 10 reveals that the default criteria for mesh refinement, gradients in the pressure or mass density, don't produce much refinement for the Cog8. As a result, the solutions and relative errors on 2D adaptive meshes are largely the same as for the base 100x100 uniform grid. This might be given the self-similar nature of the Cog8 problem; once the grids refine the initial conditions, no new grid is added.
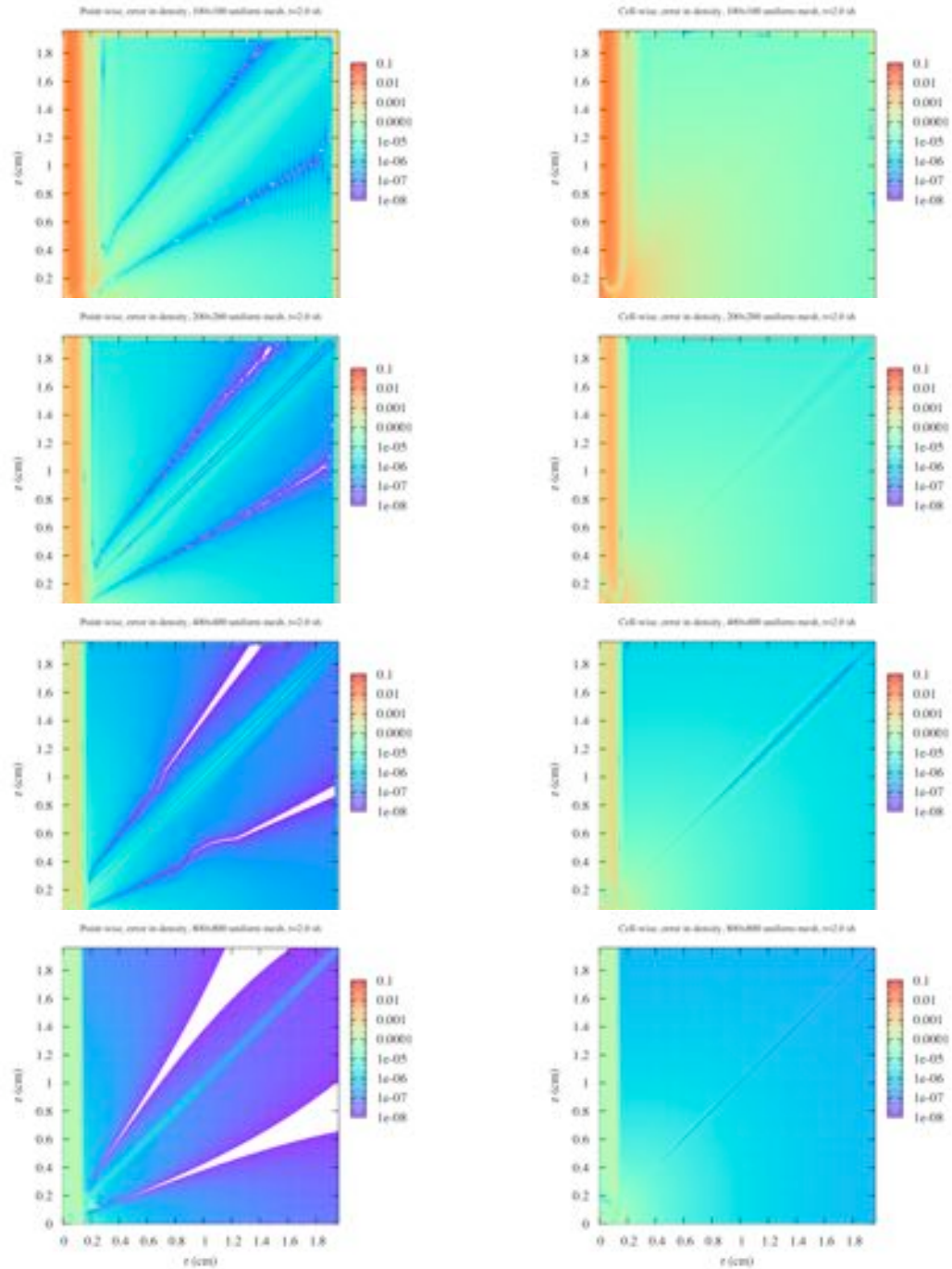
Figure 8. - Absolute values of the relative errors for a point-wise solution (left) and cell averaged solution (right) on 100x100, 200x200, 400x400, and 800x800 uniform grids at t=20 sh.
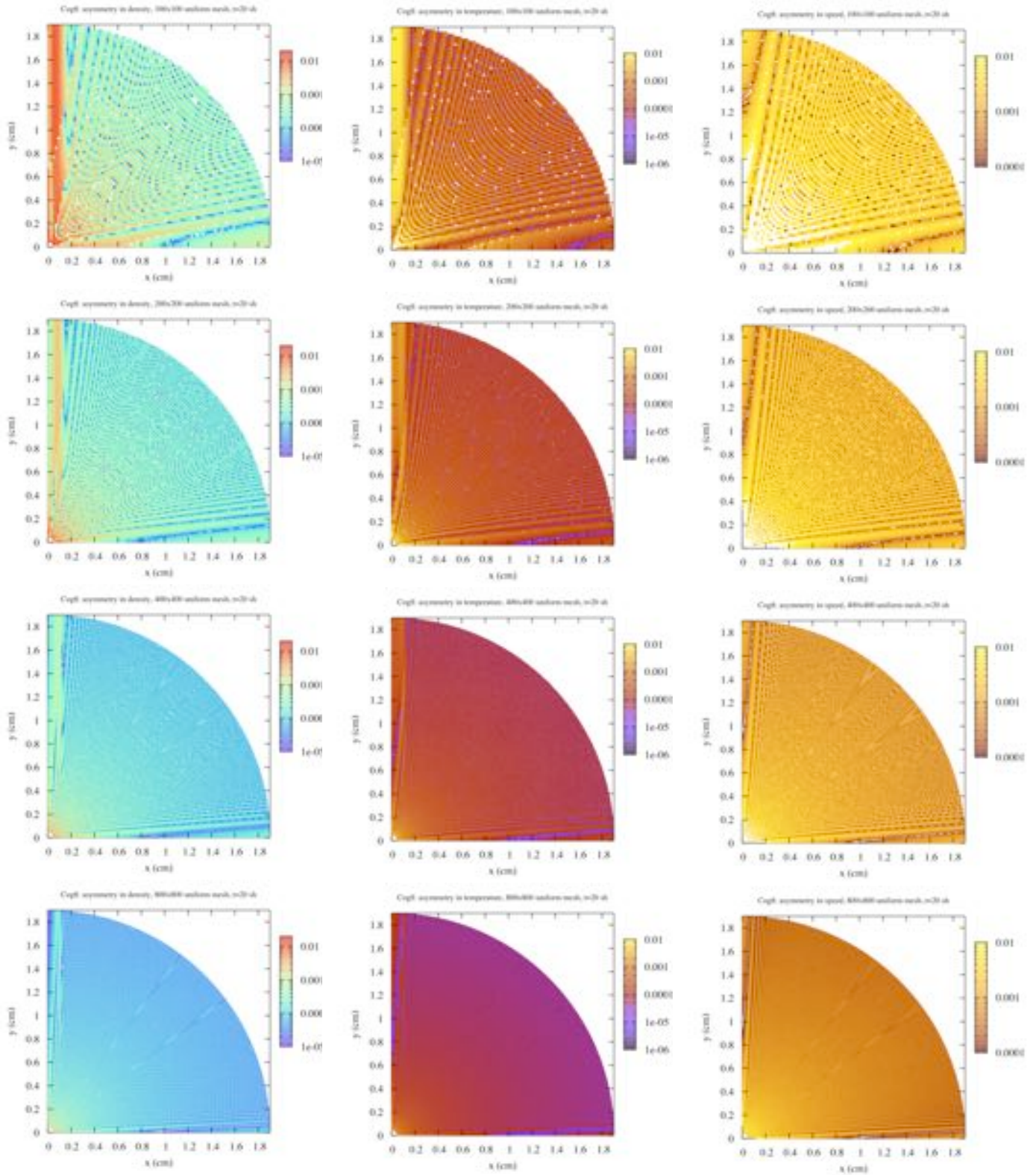
Figure 9. - Asymmetries in the numerical solutions of the Cog8 problem for the density (left), temperature (middle) and material speed (right) 100x100, 200x200, 400x400, and 800x800 uniform grids at t=20 sh.
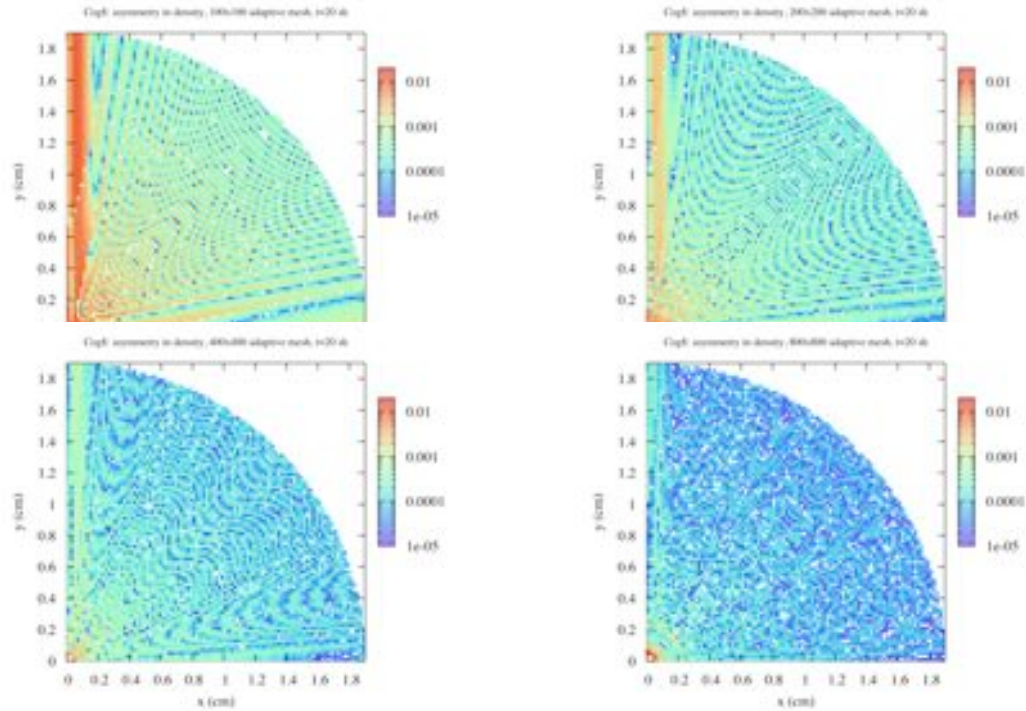
Figure 10. - Asymmetries in the numerical solution of the Cog8 test problem for the density on adaptive grids with potential maximum resolutions of 100x100, 200x200, 400x400, and 800x800 adaptive grids at t=20 sh.

2.3 The Mader Problem

The simplest test of detonation is the one-dimensional gamma-law rarefaction wave burn, for which a slab of material is initiated on one side and a detonation propagates to the other side. For a Chapman-Jouget detonation speed of 0.8 cm/μs, it takes 6.25 μs for the detonation to travel 5 cm. The rich structure of a multi-dimensional detonation is absent in the one-dimensional test problem, and a simple rarefaction wave follows the detonation front (Fickett & Davis 1979). Expansion of material in the rarefaction depends on the boundary condition where the detonation is initiated, which is usually modeled as a freely moving surface or a moving piston. For the Mader problem, a stationary piston is used. In this case, the head of the rarefaction remains at the detonation front since the flow is sonic there, and the tail of the rarefaction is halfway between the front and the piston. Care must be taken to use as thin an initiator region as possible in the input deck; otherwise a break in the rarefaction wave occurs (Kirkpatrick, Wingate & Kamm 2004). A succinct description of the Mader problem for the Tri-Lab Verification Test Suite, fortran code for generating solutions, and the spatial and temporal convergence properties are discussed elsewhere (Kamm & Kirkpatrick 2004; Timmes, Gisler & Hrbek 2005; and Timmes, Fryxell & Hrbek 2006).
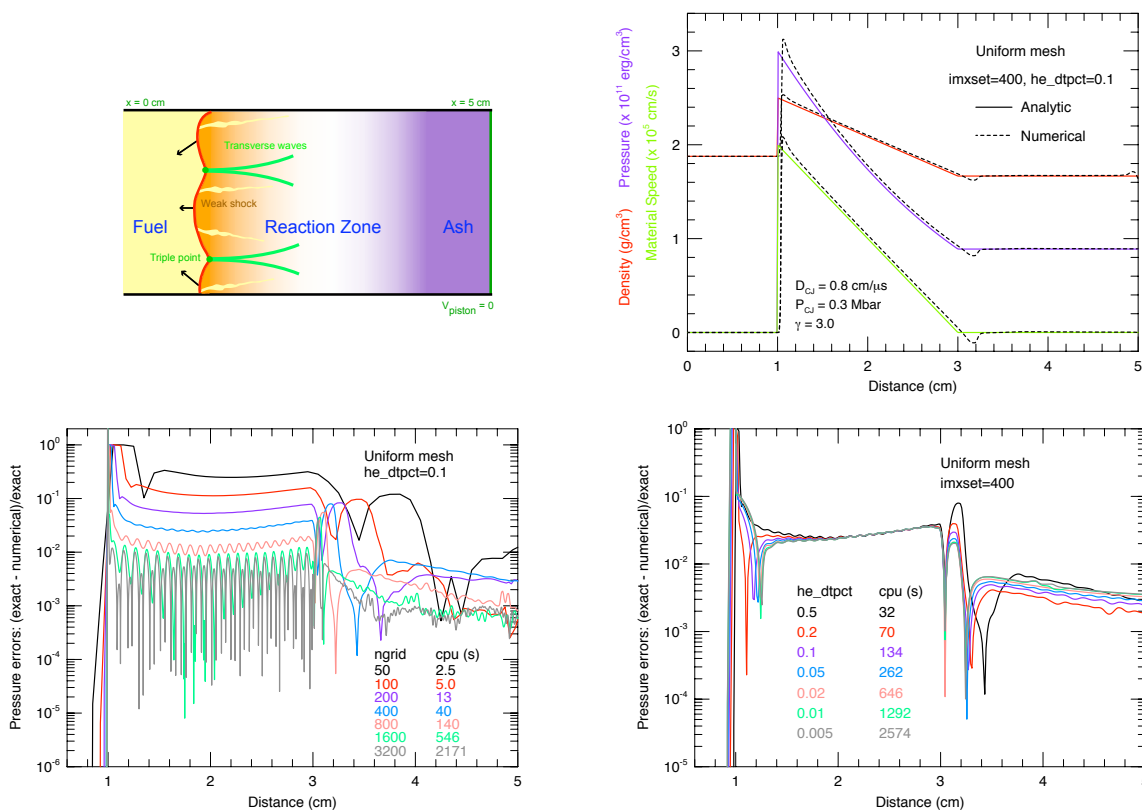
Figure 11. - Summary of the Mader problem in 1D. Shown are the basic setup (upper left), numerical and analytical solutions (upper right), relative errors in the pressure for a variety of uniform grids at a fixed time-step (lower left), and the relative error in the pressure for a variety of time-step control values on a fixed uniform grid.

Figure 11 displays a summary of the one-dimensional version of the Mader problem. The setup is illustrated in

the upper left. A representative solution on a uniform mesh of 400 cells with a time-step controller of he_dtpct=0.1 is shown in the upper right at the final time of t= 5.0 μs . Analytical and numerical solutions are overlayed for the mass density, pressure, and material speed. Even at this visual level of comparison, it is apparent that the numerical solution lags behind the analytical solution at this spatial resolution.

The image in the lower left of Figure 11 discloses the absolute value of the relative errors in the pressure for a variety of uniform grids at the final time of 5.0 μs. The parameter he_dtpct sets the maximum relative temperature change allowed per time-step in high explosive material, and determines the time-step in the numerical solution of the Mader problem. he_dtpct was set to its default value of 0.1 in limiting temperature changes to a maximum of 10% in one time-step. Cusps are due to changes of sign in the relative error, and the relative cpu cost on a single processor of increasing the spatial resolution is given. Except at the x=1.0 cm detonation front, the errors get smaller with increasing uniform grid resolution. The pressure, density (not shown), and material speed (not shown) all have roughly linear convergence rates that become smaller with increasing spatial resolution at this time-step control setting.

The image in the lower right of Figure 11 reveals the absolute value of the relative errors in the pressure for a variety of time-step control values on a uniform grid of 400 cells. The relative cpu cost on a single processor of increasing the temporal resolution is given. Values of he_dtpct $\geq$ 0.2 tend to produce inaccurate results near the detonation front and in the constant-state region x $\geq$ 3.0 cm. The pressure, density (not shown), material speed (not shown) all have a convergence rate of $\beta \sim 0$ at these spatial resolutions. That is, the L$_1$ norms for Mader problem appear largely independent of the chosen time-step, suggesting that persistent spatial inaccuracies dominate the overall error budget.

Failure of the detonation front to reach x=1 cm after 5 μs, along with difficulty in finding the temporal asymptotic regime, may derive from the parameters used in the Forest-Fire model, a global reaction kinetics model for the high-pressure chemical decomposition of heterogeneous explosives (Mader 1997). The Forest-Fire model parameters were supposedly calculated for a uniform grid spacing of 0.025 cm, 200 cells for a 5 cm domain, (Kamm & Kirkpatrick 2004, K. New, private communication 2005). Even at this spatial resolution, the detonation front fails to reach the correct x=1 cm location. At a grid spacing of 0.0015625 cm, or 3200 points, there begins to be sufficient resolution for the detonation to reach the correct position. It is well known, however, that the parameters of Forest-Fire model are cell size and equation of state dependent quantities (Mader 1997), which presents serious difficulties for performing verification studies on adaptive meshes. In addition, we couldn't find anyone who could (or would) state with certainty how the model parameters are to be derived. If the purpose of this test problem in the Tri-Lab Verification Test Suite is to verify detonation wave physics, then there are detonation problems which have far less idiosyncrasies. If the purpose of the test problem is to verify HE burn models, then additional plans are needed since NOBEL is essentially an unsupported product that hasn't had a new release since 2005.

Figure 12 exhibits four frames from a movie of the density for the Mader problem on a 200x200 uniform mesh. At a visual level of comparison, the intrinsic one-dimensionality of the test problem is apparent; at any value of the y-coordinate the pressure is commensurate with the one-dimensional values indicated by Figure 11. There is no obvious visual signs of the intrinsic cellular nature of a 2D detonation, but this may be because a initial perturbation in the density wasn't applied and/or the problem wasn't run long enough for the cellular nature to develop.

In the left column of Figure 13 is the numerical solution for the density on uniform grids of 100x100, 200x200, 400x400, and 800x800 at the final time of t=5.0 μs. In the viewgraph norm, the problem appears to remain one-dimensional. The width of the rarefaction's tail region, where the transition to a constant state is made at 3.0 cm, becomes thinner as the spatial resolution is increased. In addition, the head of the detonation gets closer to the correct x=1.0 cm position as the resolution increases.
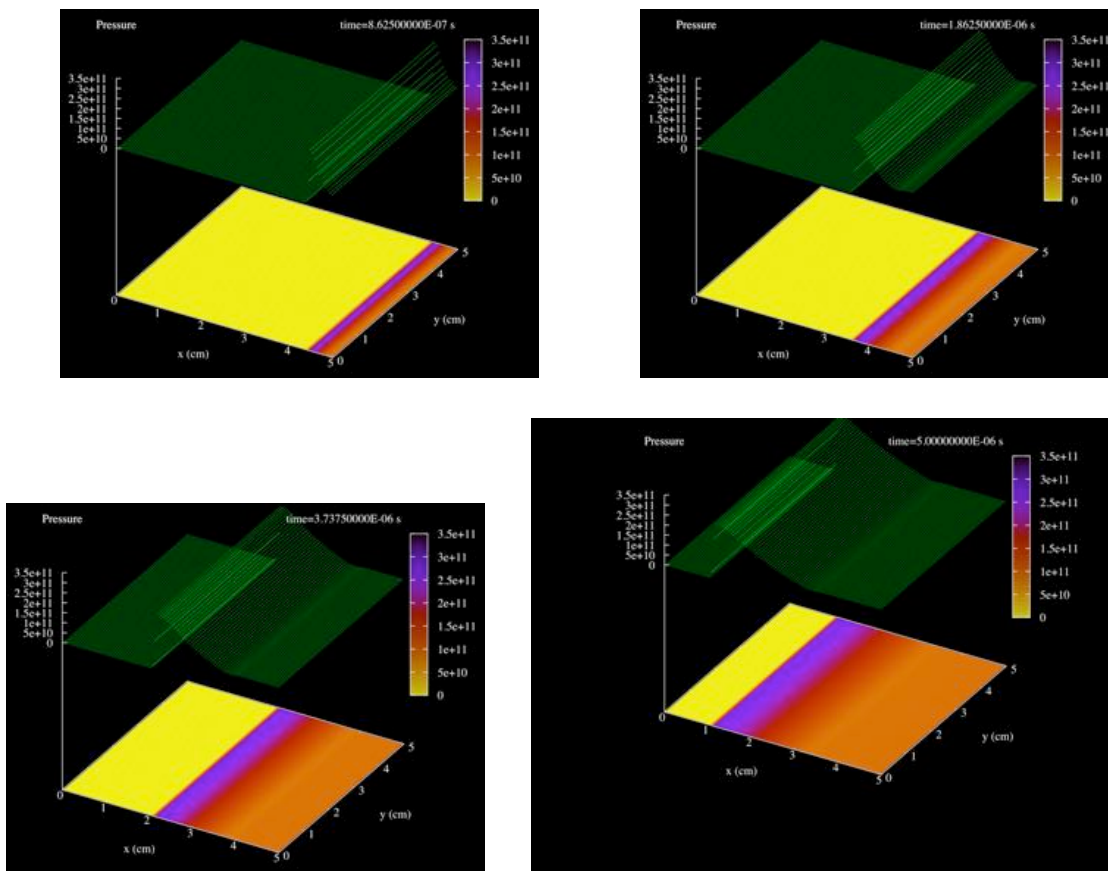

Figure 12.   - Frames from a movie of the pressure density evolution on a 200x200 uniform grid with a time-step control value of he_dtpct=0.1.

The middle column of Figure 13 details the relative error in the density for the same set of uniform grids and ending time. The largest errors occur at the head of the detonation front and in the tail region of the detonation, independent of resolution. The distribution of relative errors appears to be one-dimensional. The right column of Figure 13 is the adaptive mesh analogue of the middle column. Dots in the figure represent the grid pints where the various solutions were computed, the color of the dot indicative of the magnitude of the density field. White areas indicate regions where there is no grid, and heavily refined areas appear as continuous color maps. The base grid from which refinement began is a uniform 100x100 mesh. This gives a visual indication of the effectiveness of adaptive

meshing on the Mader problem. Note that errors are generally larger on adaptive grids, particularly in the region between the head and tail of the Taylor wave.

Figure 14 shows the solutions and relative errors for the pressure, while Figure 15 gives the same information for the material speed. Curiously, the pressure variable possesses a clumping of the relative errors in the constant region on both uniform and adaptive grids. As for the density, the largest relative errors appear at the head and tail regions of the rarefaction wave.

Table 5 details the convergence properties for the Mader problem on 2D uniform grids, while Table 6 lists the same information for adaptive grids. For uniform grids, the density, pressure, and material speed are in the spatial asymptotic regime with roughly linear convergence rates at this time-step control setting. For adaptive grids, the L_1 error norms are larger and the convergence rates are smaller, $\alpha \sim 0.5$. Thus, adaptive grids produce significant computational efficiencies for the Mader problem in 2D at the expense of a reducing convergence rate.

Table 5
Spatial Convergence Coefficients for the Mader Problem on 2D Uniform Grids

# of cells	Density $L_{1,abs}$	α	A	Pressure $L_{1,abs}$	α	A	Speed $L_{1,abs}$	α	A
100x100	5.313E-02			1.621E+10			1.308E+04		
200x200	2.785E-02	9.319E-01	8.666E-01	8.349E+09	9.570E-01	2.849E+11	6.628E+03	9.806E-01	2.469E+05
400x400	1.434E-02	9.582E-01	9.548E-01	4.160E+09	1.005E+00	3.400E+11	3.219E+03	1.042E+00	3.097E+05
800x800	7.270E-03	9.795E-01	1.048E+00	1.871E+09	1.153E+00	6.498E+11	1.397E+03	1.205E+00	6.311E+05

Table 6
Spatial Convergence Coefficients for the Mader Problem on 2D Adaptive Grids

maximum # of cells	total # of cells	Density $L_{1,abs}$	α	A	Pressure $L_{1,abs}$	α	A	Speed $L_{1,abs}$	α	A
100x100	10000	5.313E-02			1.621E+10			1.308E+04		
200x200	35704	4.223E-02	3.314E-01	1.434E-01	1.212E+10	4.191E-01	5.688E+10	1.025E+04	3.519E-01	3.754E+04
400x400	32440	2.848E-02	5.682E-01	3.434E-01	8.630E+09	4.901E-01	7.390E+10	6.852E+03	5.809E-01	8.736E+04
800x800	34072	2.296E-02	3.109E-01	1.112E-01	6.197E+09	4.777E-01	7.000E+10	5.303E+03	3.698E-01	3.463E+04

Figure 16 reveals the asymmetry in the numerical solutions of the density (left column), pressure (middle column), and material speed (right) column on uniform grids of of 100x100, 200x200, 400x400, and 800x800 at the final time of t=5.0 μs. No reference to the analytical solution is made for these plots; they are an analysis of only the symmetry in the numerical solution. For any value of the x-coordinate, the y-averaged value of a given field was determined. The color maps then express the relative difference between the field and its y-averaged value, yielding the deviations from slab symmetry. The asymmetries are the smallest ahead of the front, with deviations at the limit of double precision arithmetic. The largest asymmetries occur in regions where the field variables are constant, with deviations

on the order of 1%. Curiously, the asymmetries in these regions are not constant across the y-coordinate. In other words, while RAGE generally performs well in keeping this 1D problem essentially 1D, there are some unexpectedly large variations in regions of constant density, constant pressure, constant material speed. Is is possible that these variations are the beginning (numerically seeded) of the the cellular nature of a detonation. Future studies should run the problem out to longer times and perhaps seed the instability from the beginning.

Figure 17 shows the pressure for a Mader problem in 3D on uniform grids of 50x50x50 and 100x100x100. At the view-graph norm, the intrinsic one-dimensional nature of the test problem is apparent; the pressure at any y- and z-coordinate is commensurate with the values indicated by Figure 11. One difficulty we faced in the analysis of the 3D problem was our inability to find a suitable visualization tool - not just for the RAGE dump files, but for an arbitrary verification analysis. Slices through planes parallel to the coordinate axes reduce the verification analysis to 2D and produce results consistent with the results presented above.

Figure 13. - Density (left), relative error in the density on uniform grids (middle), and relative errors in the density on adaptive grids for the Mader problem on 100x100, 200x200, 400x400, and 800x800 grids (top to bottom) at t=5.0 μs.
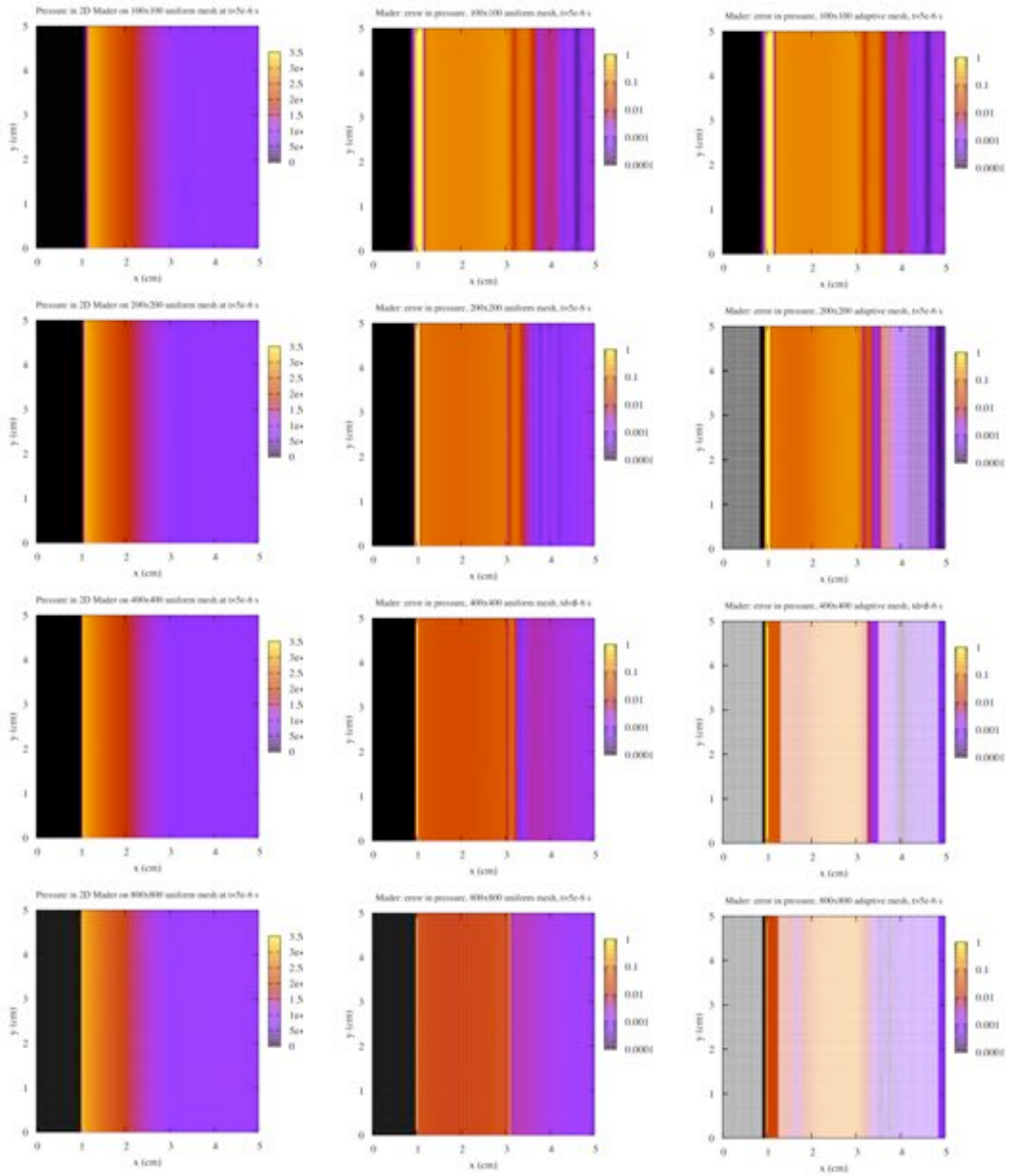
Figure 14. - Pressure (left), relative error in the pressure on uniform grids (middle), and relative errors in the pressure on adaptive grids for the Mader problem on 100x100, 200x200, 400x400, and 800x800 grids (top to bottom) at t=5.0 µs.
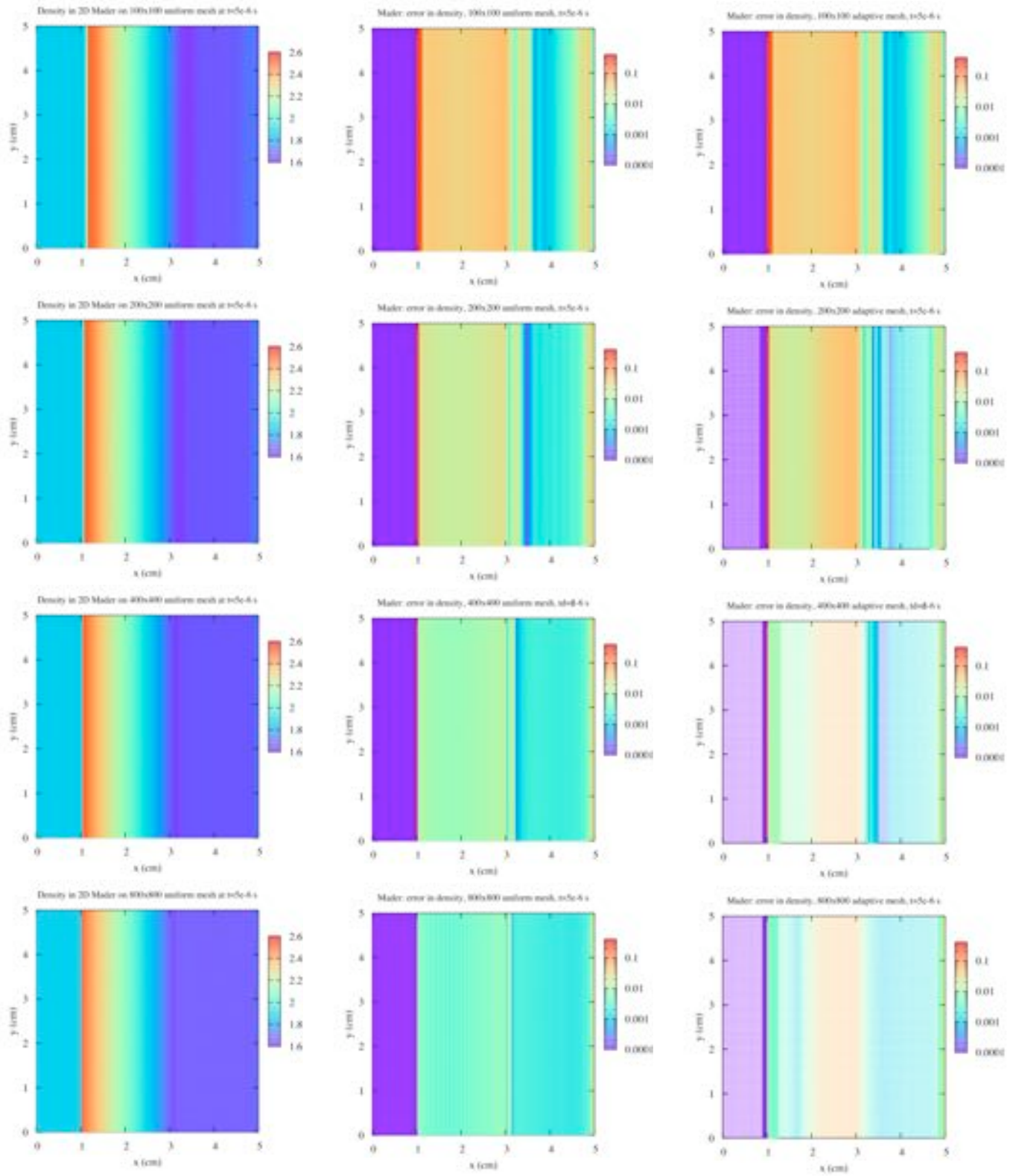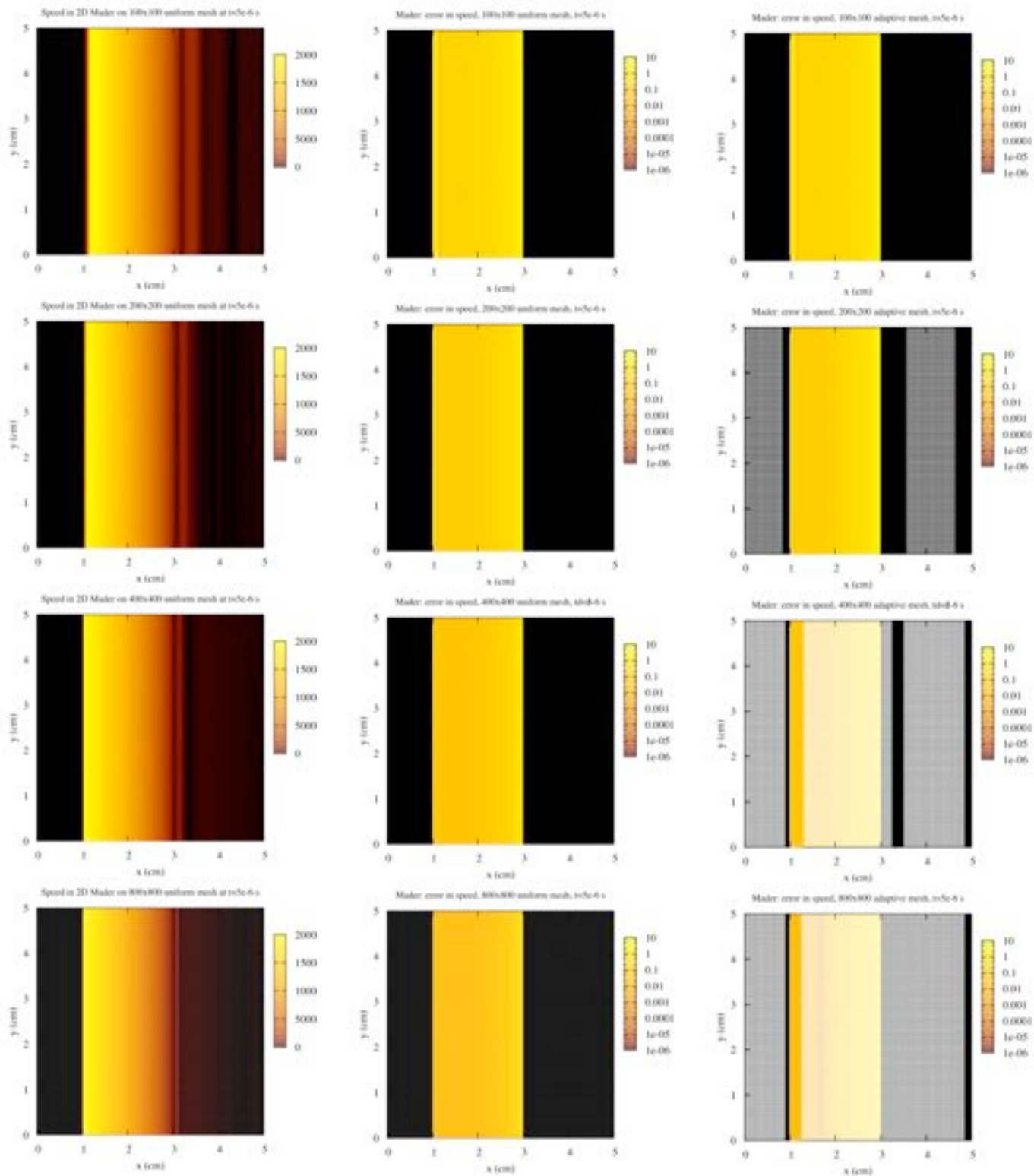
Figure 15. - Material speed (left), relative error in the speed on uniform grids (middle), and relative errors in the speed on adaptive grids for the Mader problem on 100x100, 200x200, 400x400, and 800x800 grids (top to bottom) at t=5.0 µs.

Figure 16. - Asymmetry in the density (left), pressure (middle) and material speed (right) for the Mader problem on 100x100, 200x200, 400x400, and 800x800 uniform grids (top to bottom) at t=5.0 µs.
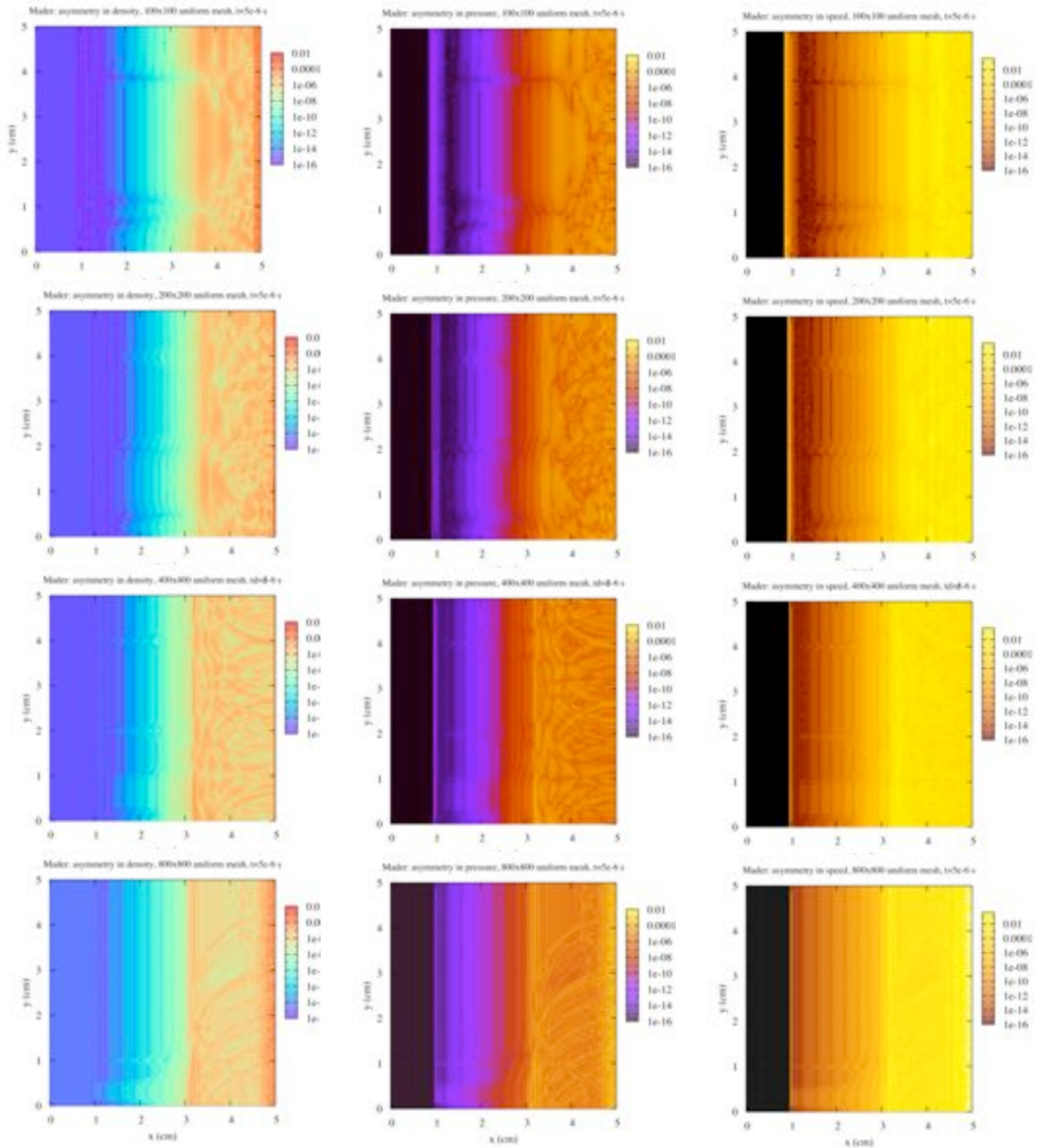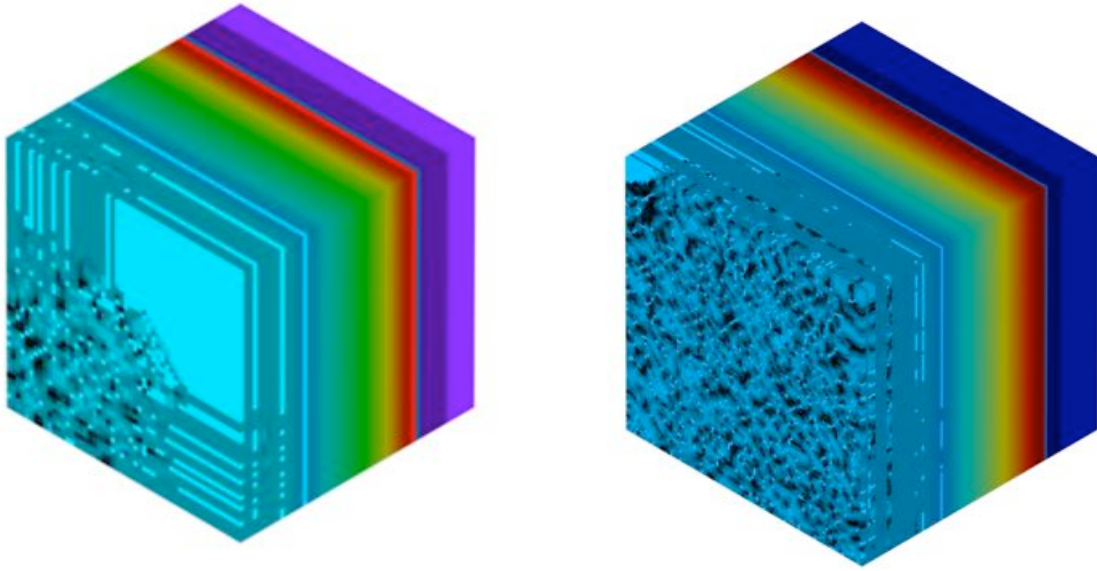
Figure 17. - Pressure for a mader problem on a 50x50x50 uniform mesh (left) and a 100x100x100 uniform mesh (right) at t=5.0 µs.

2.4 The Reinicke & Meyer–ter–Vehn Problem

The Reinicke Meyer-ter-Vehn (1991, henceforth RMTV) problem in the Tri-Lab Verification Test Suite has an initial concentrated energy source of sufficient magnitude so that heat conduction dominates the fluid flow. That is, a thermal front leads a hydrodynamic shock. The other case, where the thermal front lags the hydrodynamic shock is not presently part of the Tri-Lab Suite. RMTV examined the self-similar case and found that the fluid equations reduced to a set of four ordinary differential equations (ODEs). Evaluation of the initial conditions and multiple-region ODE integrations gives the RMTV problem has the distinction of possessing the most complicated `analytical' solution in the Tri-Lab Test Suite. Nevertheless, this problem is useful for verifying the coupling between time-dependent thermal conduction and shock hydrodynamics (Clover, Kamm, Rider, 2000; Kamm 200a). A succinct description of the RMTV problem for the Tri-Lab Verification Test Suite, fortran code for generating solutions, and the spatial and temporal convergence properties are discussed in Timmes, Gisler & Hrbek (2005) and Timmes, Fryxell & Hrbek (2006).
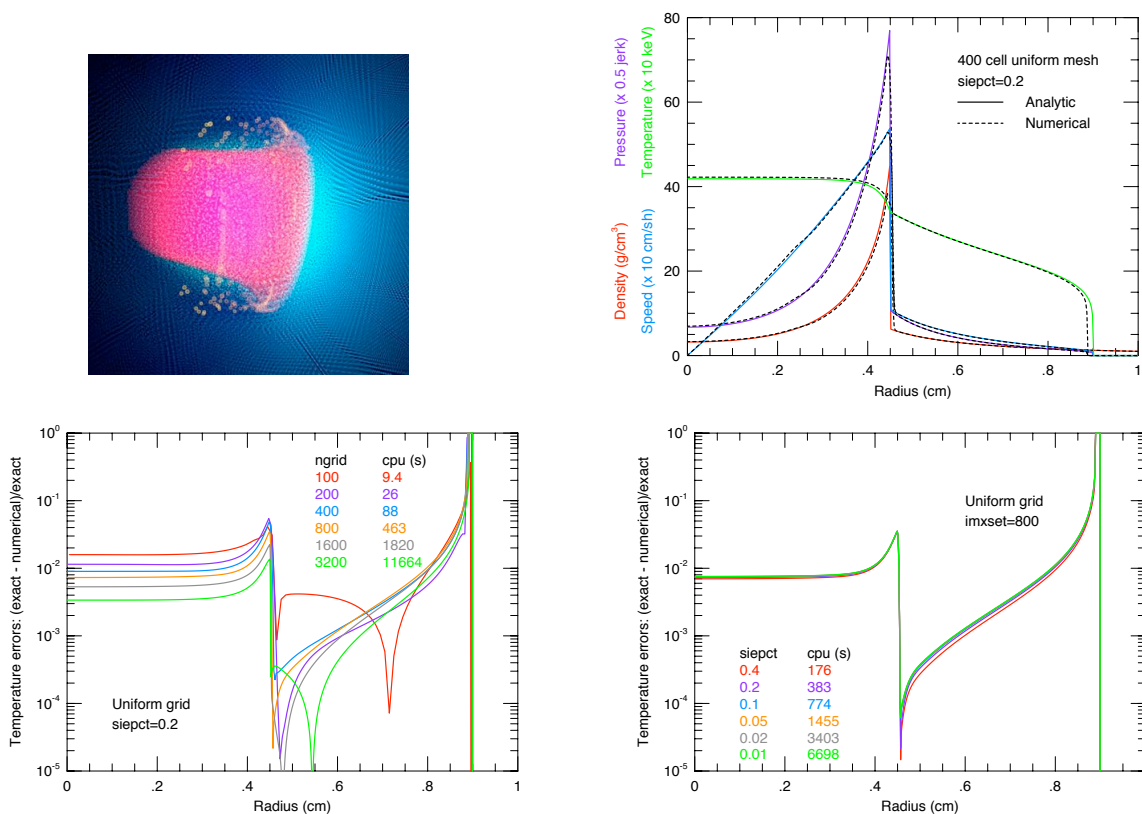
Figure 18.   - Summary of the RMTV problem in 1D. Shown are smooth particle hydrodynamics visualization of a supercritical shock, where a thermal front leads the hydrodynamic shock (upper left), numerical and analytical solutions (upper right), relative errors in the temperature for a variety of uniform grids at a fixed time-step (lower left), and the relative error in the temperature for a variety of time-step control values on fixed uniform grids.

Multi-dimensional versions of the RMTV problem wouldn't have been possible without the development a new

initialization module for RAGE (Timmes & Clover 2006). The new module provides an accurate and smooth initial state, which is particularly important for verification analyses on adaptive meshes.

Figure 18 displays a representative solution on a 800 cell uniform mesh with a time-step controller of siepct=0.2 in the upper right at the final time of t= 5.125×10^{-10} s. Analytical and numerical solutions are overlayed for the mass density, pressure, temperature and material speed. The analytic and numerical solutions reasonably agree at this level of visual comparison, although there is a difference in the location of the thermal front's leading edge (green curve) at this spatial resolution.

The image in the lower left of Figure 18 displays the absolute value of the relative errors in the temperature for a variety of uniform grids at the final time of 5.125×10^{-10} s. The parameter siepct sets the maximum fractional change in the specific internal energy per time-step. It also determines the time-step in the numerical solution of the RMTV problem and was set at its default value of 0.2, limiting changes in any cell's specific internal energy to 20% in a time-step. The relative cpu cost on a single processor of increasing the spatial resolution is given. Large persistent errors exist at the leading edge of the thermal front at x=0.9 cm and at the shock front at 0.45 cm. Other cusps are due to changes of sign in the relative error. In the region between the origin and shock at 0.45 cm the errors generally decrease with increasing spatial resolution, but fail to follow a clear pattern. In the region between the shock front at 0.45 cm and the thermal front at 0.90 cm the errors associated with the density solution saturate (not shown), but the temperature and velocity errors (not shown) increase (!) with increasing resolution.

The image in the lower right of Figure 18 reveals the absolute value of the relative errors in the temperature for a variety of time-step control values on a uniform grid of 800 cells. The relative cpu cost on a single processor of increasing the temporal resolution is given. The density, pressure, temperature, and material speed all have a convergence rate of $\beta \sim 0$ at these spatial resolutions. That is, the L_1 norms for RMTV problem appear largely independent of the chosen time-step, suggesting the error budget is dominated by the spatial errors from the heat front and shock.

In the left column of Figure 19 is the numerical solution for the density on uniform grids of 100x100, 200x200, 400x400, and 800x800 at the final time of t=5.125×10^{-10} s. As the spatial resolution is increased, the width of the density peak, which marks the hydrodynamic shock, becomes thinner and more symmetrical. The location of the shock front at r=0.45 cm is in visual agreement with the one-dimensional values of Figure 19.

The middle column of Figure 19 displays the relative error in the density (compared to the analytical solution) for the same set of uniform grids and ending time. In general, the errors are about 10^{-4} - 10^{-5}. There are non-zero errors ahead of the density peak because the thermal front is ahead of the hydrodynamic front. Cusps are due to changes of sign in the relative error and are easily visible as the blue valleys, one starting from the z-axis and a second starting on the r-axis. The images aren't symmetric at any spatial resolution, suggesting the underlying numerical solution isn't axisymmetric. In addition, the relative error in the density is larger for locations near the z-axis than for points near the r-axis. For these uniform grids Table 7 reveals the global L_1 error norm decreases as the spatial resolution increases at a rate consistent with linear convergence.

The right column of Figure 19 is the adaptive mesh analogue of the middle column. The base grid from which refinement began is a uniform 100x100 mesh. The maximum spatial resolution of each adaptive mesh is set equal to the uniform mesh counterpart. Dots in the figure represent the grid pints where the various solutions were computed,

Figure 19. - Density (left), relative error in the density on uniform grids (middle), and relative errors in the density on adaptive grids for the RMTV problem on 100x100, 200x200, 400x400, and 800x800 grids (top to bottom) at t=5.125×10⁻¹⁰ s
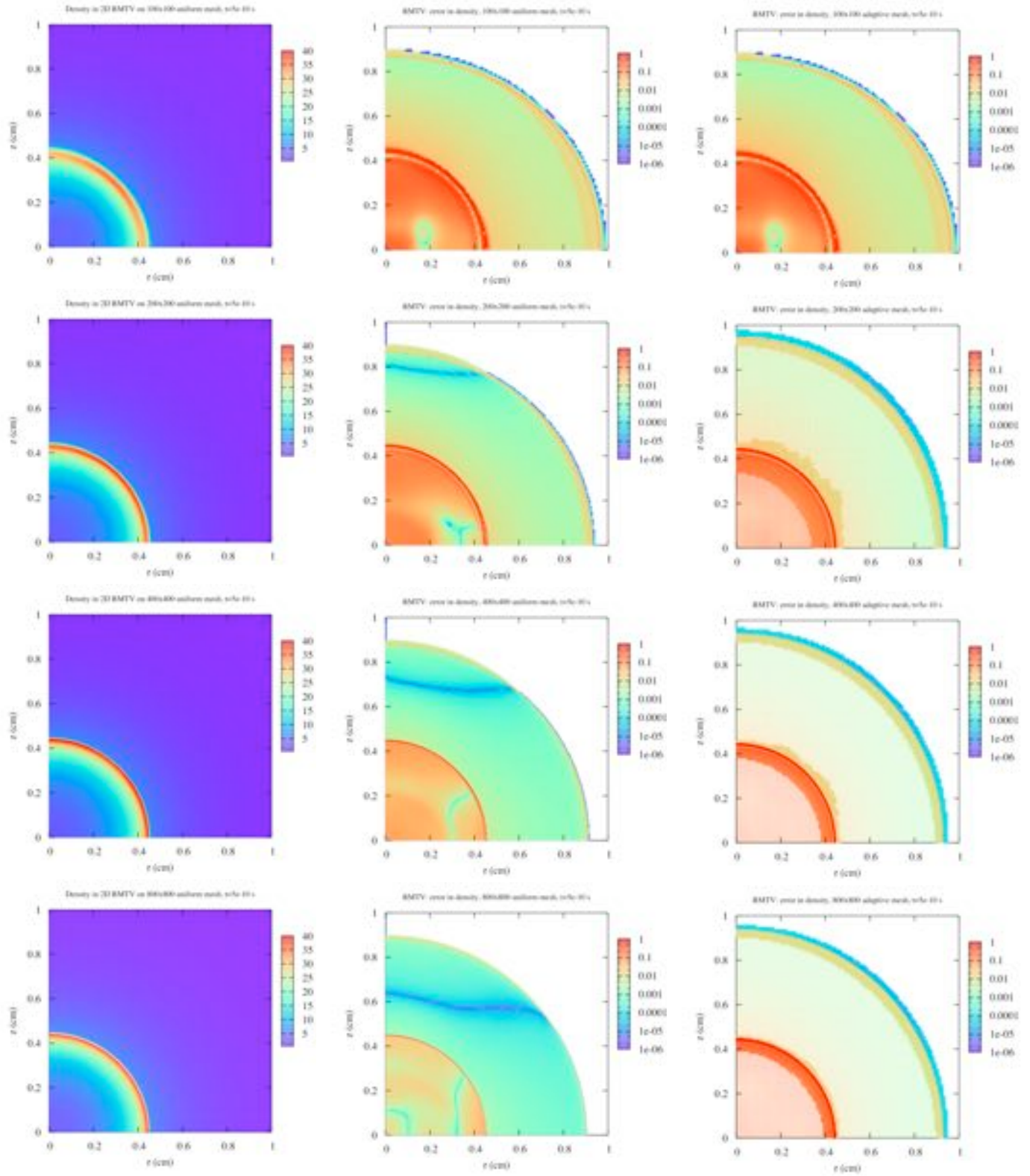
Figure 19. - Density (left), relative error in the density on uniform grids (middle), and relative errors in the density on adaptive grids for the RMTV problem on 100x100, 200x200, 400x400, and 800x800 grids (top to bottom) at $t=5.125\times10^{-10}$ s

the color of the dot indicative of the magnitude of the density field. White areas indicate regions where there is no grid, and heavily refined areas appear as continuous color maps. This gives a direct visual indication of the effectiveness of adaptive meshing on the RMTV problem. However, this efficiency gain isn't generally accompanied by a corresponding reduction in the difference between the numerical and analytical solutions. In fact, the errors on adaptive grid solutions are larger than the errors on corresponding uniform grids. On uniform grids, for example, the region between the heat front and the shock is blueish indicating a smaller relative error. On the adaptive grids this region is redder indicating larger errors. Note the odd refinement features near the shock front. For these adaptive grids Table 8 demonstrates the global L_1 error norm increases as the spatial resolution increases. That is, the solutions on adaptive grids are not as accurate as the solutions on uniform grids. This is probably an artifact of RAGE's adaptive grid refinement algorithm.

Table 7
Spatial Convergence Coefficients for the RMTV Problem on 2D Uniform Grids

# of cells	Density $L_{1,abs}$	α	A	Pressure $L_{1,abs}$	α	A
100x100	3.055E-01			1.377E+16		
200x200	1.376E-01	1.151E+00	6.117E+01	6.178E+15	1.156E+00	2.822E+18
400x400	7.003E-02	9.745E-01	2.404E+01	2.879E+15	1.101E+00	2.116E+18
800x800	3.846E-02	8.648E-01	1.246E+01	1.517E+15	9.248E-01	7.341E+17

# of cells	Temperature $L_{1,abs}$	α	A	Speed $L_{1,abs}$	α	A
100x100	1.591E+02			6.127E+06		
200x200	6.643E+01	1.260E+00	5.256E+04	2.630E+06	1.220E+00	1.688E+09
400x400	3.030E+01	1.133E+00	2.682E+04	1.279E+06	1.041E+00	6.521E+08
800x800	1.476E+01	1.038E+00	1.518E+04	6.919E+05	8.861E-01	2.585E+08

Table 8
Spatial Convergence Coefficients for the RMTV Problem on 2D Adaptive Grids

maximum # of cells	total # of cells	Density $L_{1,abs}$	α	A	Pressure $L_{1,abs}$	α	A
100x100		3.055E-01			1.377E+16		
200x200		4.145E-01	-4.401E-01	4.026E-02	1.806E+16	-3.916E-01	2.268E+15
400x400		5.541E-01	-4.186E-01	4.511E-02	2.291E+16	-3.430E-01	2.934E+15
800x800		6.901E-01	-3.168E-01	8.303E-02	2.760E+16	-2.690E-01	4.570E+15

maximum # of cells	total # of cells	Temperature $L_{1,abs}$	α	A	Speed $L_{1,abs}$	α	A
100x100	10000	1.591E+02			6.127E+06		
200x200	18548	1.774E+02	-1.576E-01	7.697E+01	6.046E+06	1.920E-02	6.694E+06
400x400	31144	2.044E+02	-2.040E-01	6.019E+01	7.390E+06	-2.896E-01	1.303E+06
800x800	54864	2.247E+02	-1.371E-01	8.985E+01	8.745E+06	-2.428E-01	1.726E+06

In the left column of Figure 20 is the numerical solution for the temperature on the same set of uniform grids and ending time as in Figure 19. There are two jumps and two plateaus in the temperature. The first jump at r=0.90 comes from the leading thermal front. Behind the thermal front is the first plateau where the temperature gradually increases toward the origin. The second jump at r=0.45 marks the location of the following hydrodynamic shock, and the second plateau is the post-shock region extending to the origin. As the spatial resolution is increased, the width of the leading temperature edge, which marks the thermal front, becomes thinner and more symmetrical.

The middle column of Figure 20 displays the relative error in the temperature for the same set of uniform grids and ending time, while the right column of Figure 20 exhibits the relative error in the temperature for adaptive grids. The cusps, indicative of a change in sign in the relative error, are asymmetrical indicating that the 2D numerical solution on uniform grids is generating some asymmetries. Like the density solution, the errors for the temperature solution on adaptive grid solutions are larger than the errors on corresponding uniform grids. For the adaptive meshes, note the odd refinement pattern near the shock front and the nearly circular cusp at a radius of $\sim$ 0.6 cm. Table 7 establishes that the temperature solution on uniform grids converges at roughly a linear rates, while Table 8 shows that the corresponding solutions on adaptive meshes become worse as the refinement level is increased. This is probably an artifact of RAGE's adaptive grid refinement algorithm.

In the left column of Figure 21 is the numerical solution for the magnitude of the material velocity vector (the material speed) for the same set of uniform grids and ending time. Behind the leading thermal front the material speed stays small with a slight increase as the hydrodynamic shock is approached. The post-shock material speed is a linear function of position back to the origin. The middle column of Figure 21 displays the relative error in the material speed for the same set of uniform grids and ending time, while the right column of Figure 21 exhibits the relative error in the material speed for adaptive grids. For both uniform and adaptive grids the relative errors for the material speed are larger than the relative errors for either the density or temperature. Like the density and temperature solutions, the errors for the material speed on adaptive grid solutions are larger than the errors on corresponding uniform grids. Table 7 demonstrates that the material speed solution on uniform grids converges at roughly a linear rate, while Table 8 shows that the corresponding solution on adaptive meshes is diverging.

Asymmetries in the numerical solutions to the RMTV problem for uniform grids are illustrated in Figure 22. Across any row is the asymmetry in the mass density, temperature and material speed. Down any column are the asymmetries on 100x100, 200x200, 400x400, and 800x800 uniform grids at the ending time t=20 sh. The color maps plot the relative difference between the field at a given radius ($\sqrt{r^2 + z^2}$) and its radially-averaged value. Such plots essentially give the deviations from spherical symmetry. Each of the fields in Figure 22 displays a strong axis of symmetry about the diagonal. The density, temperature, and material speed all have their largest asymmetries, relative to the mean radially average value, at locations near the z-axis. In fact, a time-elapsed movie of the RMTV problem uncovers the fact that for times t$\leq$ 3$\times$10^{-10} s the heat and shock fronts travel along locations near the z-axis faster than for locations along the r-axis, yielding an ellipsoidal shaped solution rather than a spherically shaped solution.

Asymmetries in the numerical solution to the RMTV problem for the density on adaptive grids are revealed in Figure 23. The adaptive grids maximum spatial resolutions are equal to their uniform grid counterparts if they become refined everywhere. The base grid from which adaptive meshing commenced was a uniform 100x100 grid. As in Figure 22, the color maps display the relative difference between a field and its radially-averaged value to reveal

asymmetries in the numerical solution. Figure 23 implies that the default criteria for mesh refinement, gradients in the pressure or mass density, produce significant refinement for RMTV. In general, the asymmetries in the uniform grid solutions are largely absent in the adaptive grid cases. Like the uniform grid case, however, the shock is asymmetric.

Figure 20. - Temperature (left), relative error in the temperature on uniform grids (middle), and relative errors in the temperature on adaptive grids (right) for the RMTV problem on 100x100, 200x200, 400x400, and 800x800 grids (top to bottom) at t=5.125×10⁻¹⁰ s

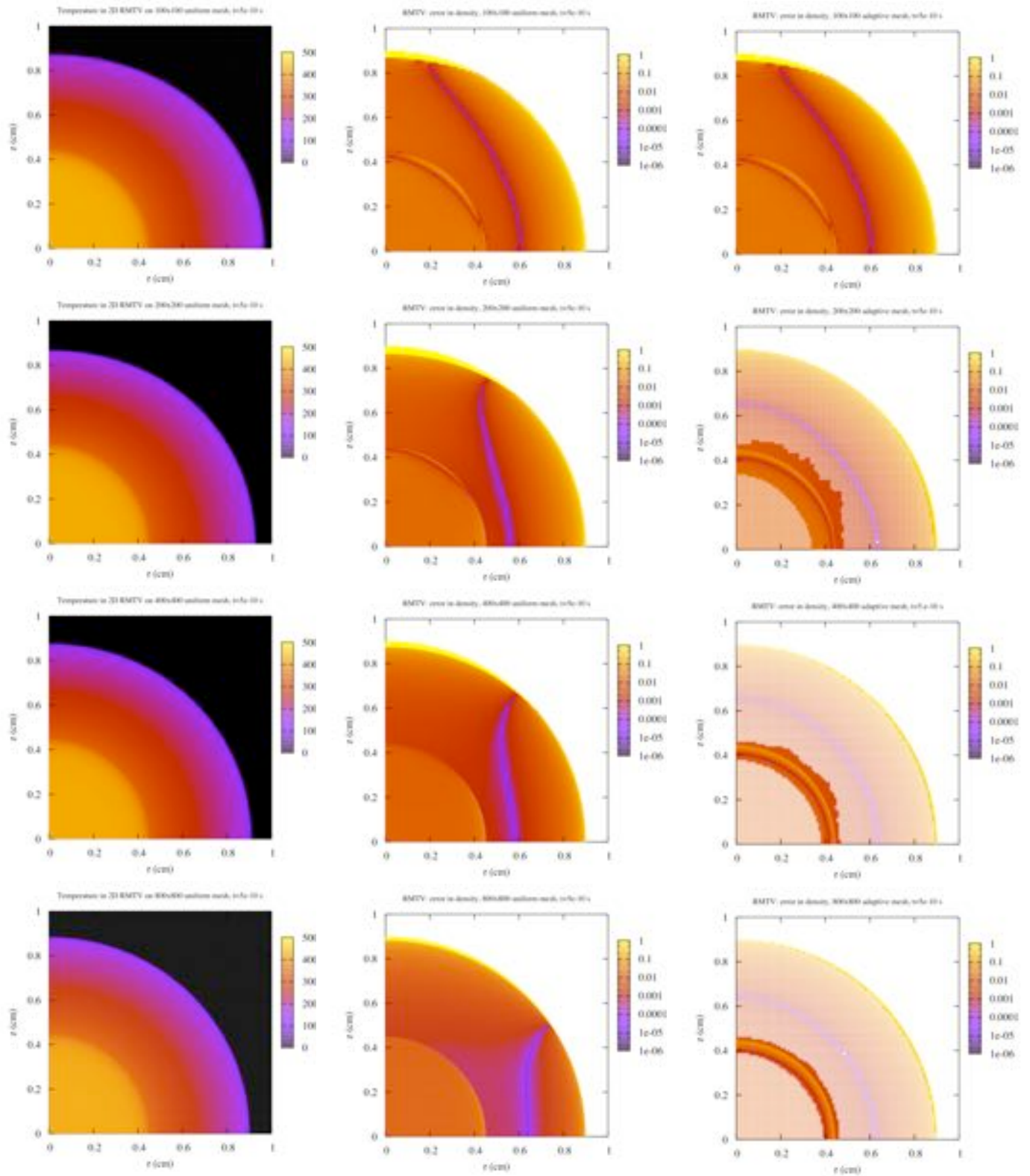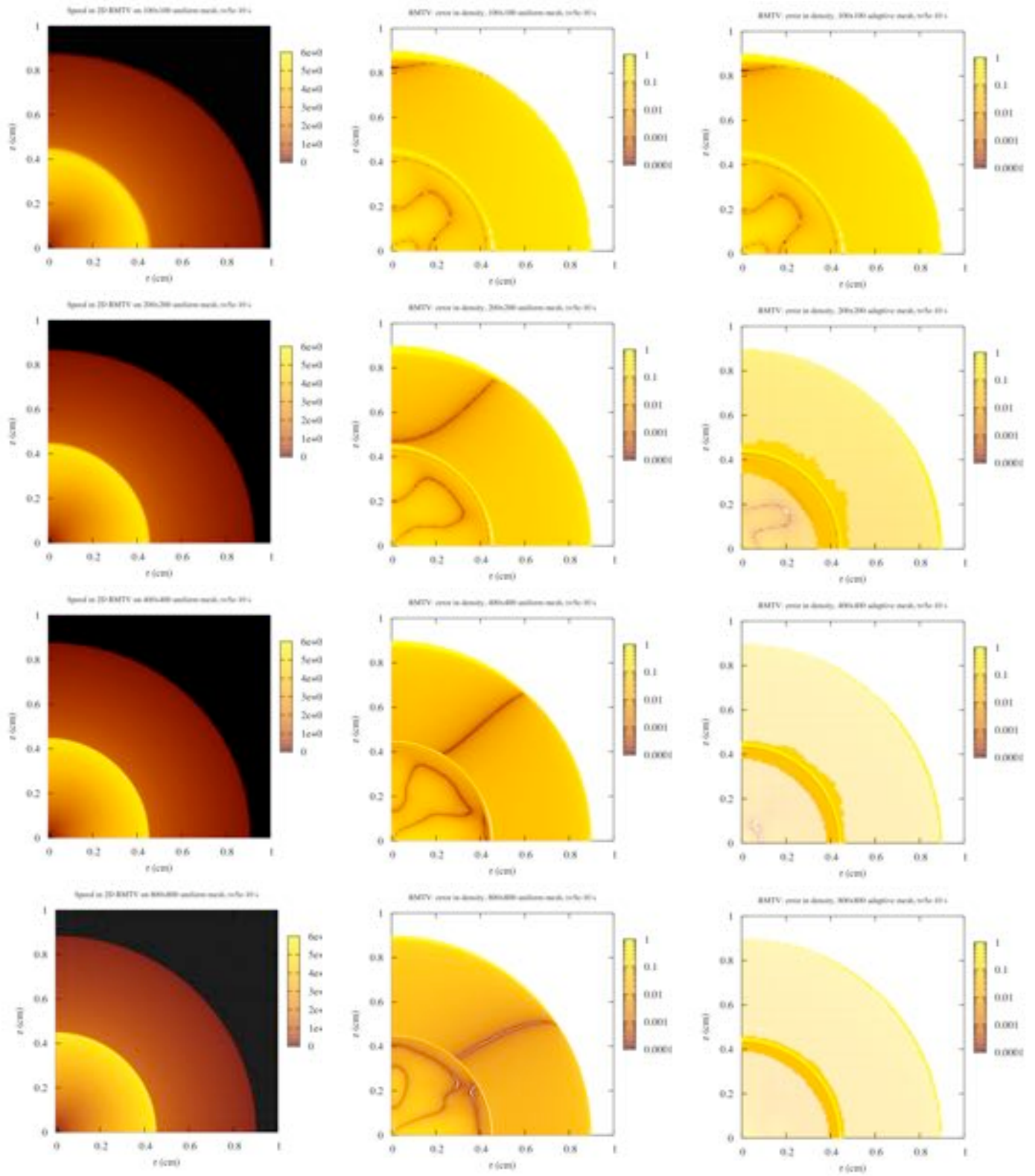*Figure 21. - Speed (left), relative error in the speed on uniform grids (middle), and relative errors in the speed on adaptive grids (right) for the RMTV problem on 100x100, 200x200, 400x400, and 800x800 grids (top to bottom) at t=5.125×10⁻¹⁰ s*

Figure 22. - Asymmetries in the numerical solution of the RMTV problem for the density (left), temperature (middle) and material speed (right) on 100x100, 200x200, 400x400, and 800x800 uniform grids at t=5.125×10⁻¹⁰ s.

Figure 23. - Asymmetries in the numerical solution of the RMTV problem for the density (left), temperature (middle), and material speed (right) on adaptive grids with potential effective resolutions of 100x100, 200x200, 400x400, and 800x800 (top to bottom) at t=5.125×10⁻¹⁰ s.
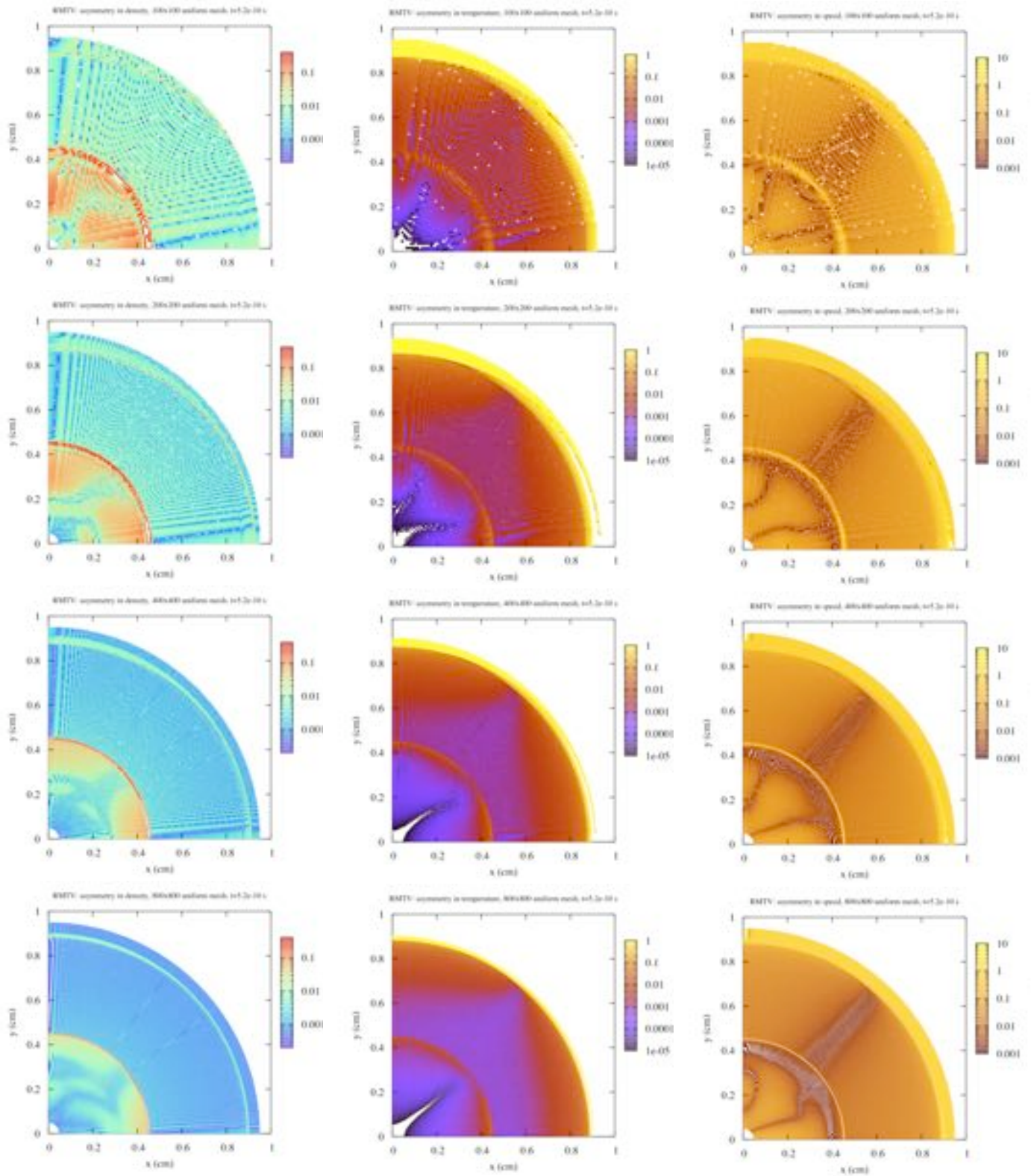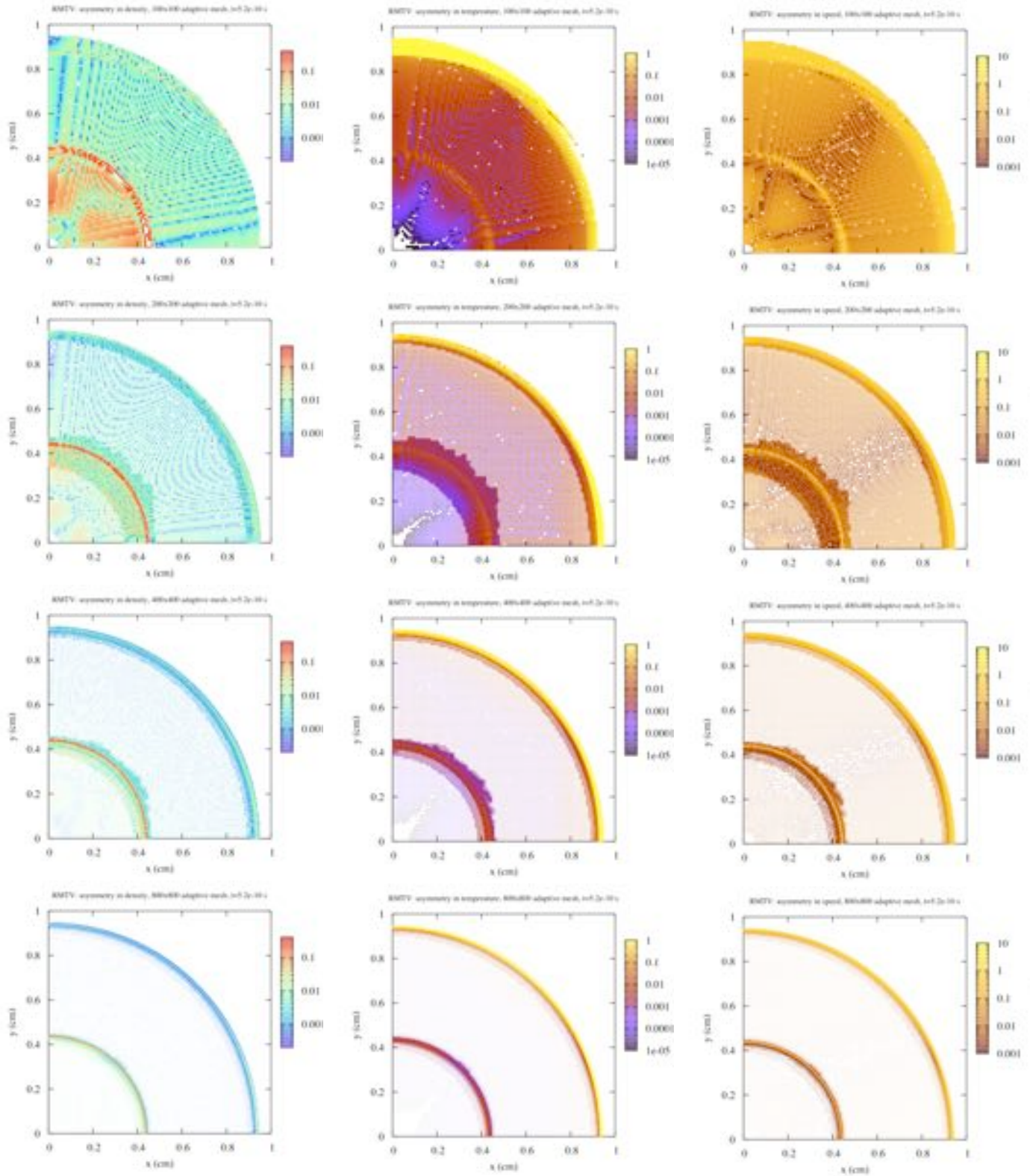
2.5 The Noh Problem

The Noh problem (Noh 1987) is a standard verification problem for hydrocodes. A gamma-law gas is initialized with a uniform, radially inward velocity. A shock forms at the origin and propagates outward as the gas stagnates. This problem tests a code's ability to transform kinetic energy into internal energy, and the ability to follow supersonic flows. The analytical solution is easy to calculate, and the convergence of the hydrocode solution can be directly determined. A succinct description of the Noh problem for the Tri-Lab Verification Test Suite, fortran code for generating solutions, and the spatial and temporal convergence properties are discussed in Timmes, Gisler & Hrbek (2005) and Timmes, Fryxell & Hrbek (2006).
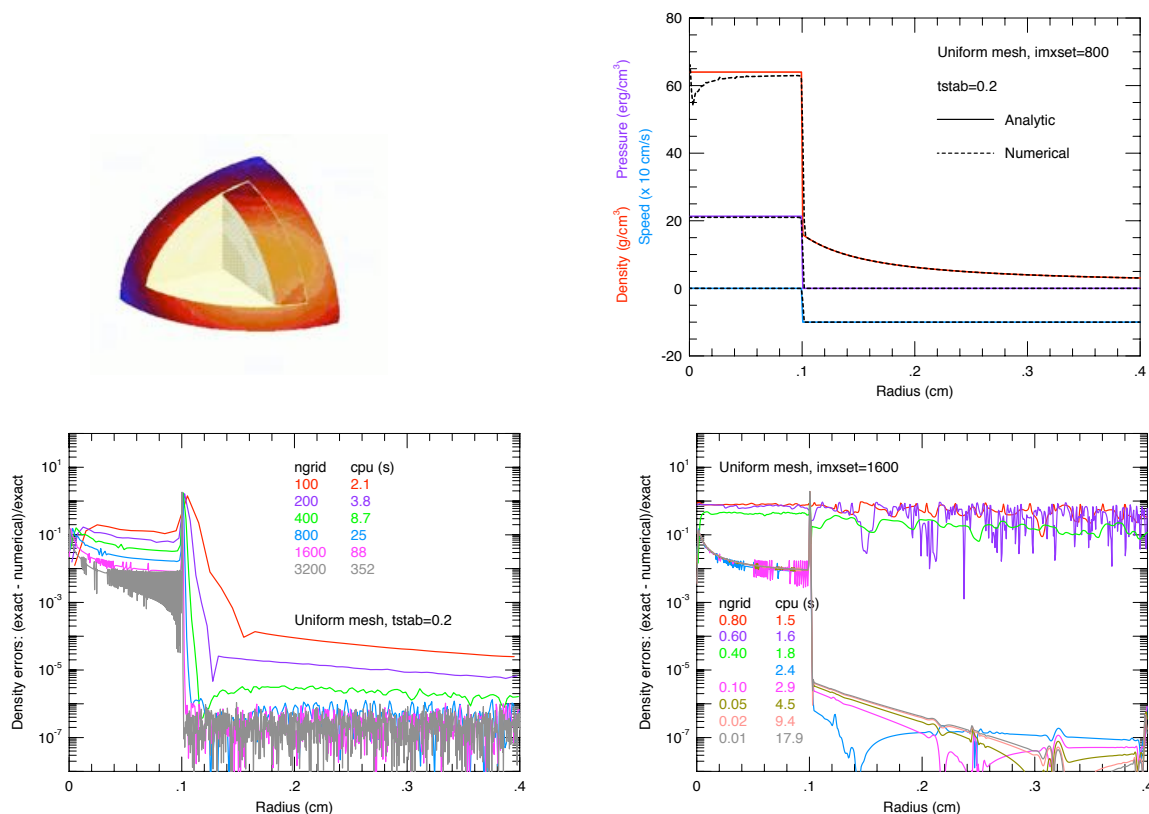
Figure 24. - Summary of the Noh problem in 1D. Shown are a 3D representation of the Noh problem (upper left), numerical and analytical solutions (upper right), relative errors in the density for a variety of uniform grids at a fixed time-step (lower left), and the relative error in the density for a variety of time-step control values on a fixed uniform grid.

Figure 24 displays a representative solution on a 800 cell uniform mesh with a time-step controller of tstab=0.2 in the upper right at the final time of t=0.3 s. Analytical and numerical solutions are overlayed for the mass density, pressure, and material speed. The analytic and numerical solutions generally agree at this level of visual comparison except near the axes. Shock reflection or shock interactions are often associated with a phenomenon known generically as wall heating (Noh 1987). RAGE, like most other hydrodynamics codes, produces the anomaly when reflecting a

shock off a boundary or focusing a shock toward the origin in a convergent geometry (Rider 200). This heating causes premature stagnation, with densities lower than predicted in the centermost cells. In Figure 19 the central zones has a stagnation density above 75 g/cc. Further out, matter stagnates at densities of 58-62 g cm^{-3}. The correct value is 64 g cm^{-3}. The extent to which the anomalous heating occurs depends on the nature of the shock reflection, so that wall heating may or may not be important for a given problem.

The image in the lower left of Figure 24 exhibits the absolute value of the relative errors in the density for a variety of uniform grids at the final time of 0.3 s. The parameter tstab sets the time step allowed by the material speed, Δt = tstab $\cdot$ Δx / ($|v_x| + |v_y| + |v_z|$), and determines the time-step in the numerical solution of the Noh problem. It was set at its default value of 0.2, limiting transport to 20% of a cell's width. The relative cpu cost on a single processor of increasing the spatial resolution is given. The large errors from the anomalous heating at the origin is evident. Persistent errors near the right boundary are probably due to the inflow boundary condition. It is encouraging, however, that between the origin and the shock there is a steady decline in the magnitude of the errors as the spatial resolution is increased. Figure 24 implies that the density, pressure, and material speed have roughly linear convergence rates ($\alpha \sim 1$), mainly due to the large persistent errors from wall-heating and the inflow boundary at this time-step control setting.

The image in the lower right of Figure 24 shows the absolute value of the relative errors in the temperature for a variety of time-step control values on a uniform grid of 1600 cells. The relative cpu cost on a single processor of increasing the temporal resolution is shown. Figure 24 shows that the density has a bimodal convergence rate. For tstab$\geq$0.2 the convergence rate in the $L_{1,abs}$ norm is near linear, while for smaller values of tstab the convergence rate is near zero. That is, the L_1 norm for the Noh problem appears largely independent of the chosen time-step below a certain level. For large values of tstab, the Noh test problem violates the recommended accuracy criterion of the code.

In the left column of Figure 25 is the numerical solution for the density on uniform grids of 100x100, 200x200, 400x400, and 800x800 at the final time of t=0.3 s. As the spatial resolution is increased, notice the stripes adjacent to and parallel to the horizontal axis within the shock region and similarly adjacent to the vertical axis. These grid aligned features are probably anomalous artifacts of RAGE's hydrodynamics. There is also a broad valley at 45°. As the spatial resolution is increased, there is a distinct sharpening of the shock interface, a narrowing of the diagonal valley feature and of the grid-aligned stripes. In the finest resolution calculation at bottom left, the pattern is distinctly that of a herringbone, with a rather broad 45 degree spine (the valley seen at lower resolution has become a hump) and narrow grid-aligned ribs.

The middle column of Figure 25 is the adaptive mesh analogue of the right column. Dots in the figure represent the grid pints where the various solutions were computed, the color of the dot indicative of the magnitude of the density field. White areas indicate regions where there is no grid (i.e., de-refinement has occurred). The base grid from which refinement began is a uniform 100x100 mesh. The maximum spatial resolution of each adaptive mesh is equal to its uniform mesh counterpart. Such plots gives a visual indication of the ineffectiveness of adaptive meshing on the Noh problem. In fact, the adaptive mesh rapidly becomes fully refined at the first cycle of the problem. This is puzzling because there are no gradients in any physical property at the first cycle. Density, pressure, and temperature are all uniform throughout the grid. The material speed is also uniform, directed radially inward, but the v_r and v_z
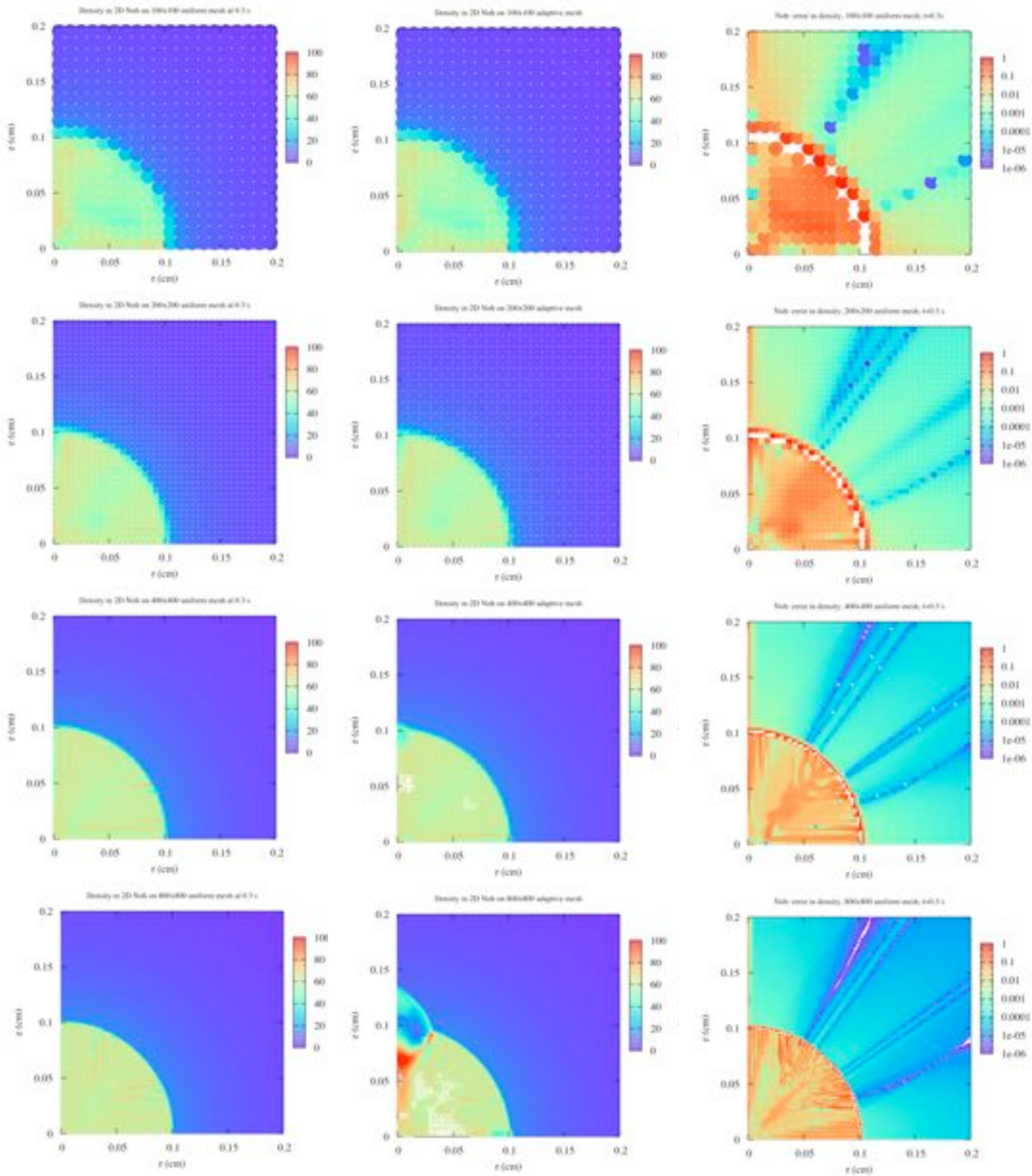
Figure 25. - Density field on uniform grids (left), density field on adaptive grids (middle) and relative error in the density on uniform grids (right) for the Noh problem. The spatial resolution is 100x100, 200x200, 400x400, and 800x800 grids (top to bottom) at t=0.3 s

velocity components separately vary from cell to cell to keep the radial velocity uniform. Examination of the relevant RAGE modules reveals that the refinement that occurs at cycle zero does indeed depend on the velocity components separately. However, the use of adaptive meshing in the Noh problem leads to very deleterious consequences regardless of (or in spite of) the initial refinement.

The middle column of Figure 25 shows that as the resolution is increased in the adaptive mesh calculations a surprising and catastrophic anomaly appears on the z- axis; a low density bubble straddling the shock. This may be related to the carbuncle phenomenon that is known to affect some Godunov schemes (Quirk 1994). Since RAGE is refining everywhere down to the finest allowed cell size on the initial time step, and the results are not identical with the uniform grid calculations, the problem must arise during de-refinement. Additional analysis reveals the z-axis bubble is seeded at one of the de-refined regions.

The difficulties discussed above were also found in last year's Tri-Lab Verification report (Timmes, Gisler & Hrbek 2005). Last year, a special version of RAGE (Gittings version 20050818.010) and a new input variable (rho_eps) which relaxes the refinement criteria, allowed the Noh problem to run on 2D adaptive mesh Noh without producing the carbuncle phenomena. Even with these fixes the total number of cells remained quite large. Apparently these special fixes haven't become part of the present version of RAGE. In addition, one can object to special fixes for generic test problems in a hydrodynamics code that strives for generality.

Table 9
Spatial Convergence Coefficients for the Noh Problem on 2D uniform grids

# of cells	Density $L_{1,abs}$	α	A	Pressure $L_{1,abs}$	α	A	Speed $L_{1,abs}$	α	A
100x100	2.593E-01			7.532E-02			3.569E-03		
200x200	1.329E-01	9.641E-01	2.198E+01	3.872E-02	9.598E-01	6.259E+00	1.826E-03	9.667E-01	3.061E-01
400x400	8.141E-02	7.073E-01	5.638E+00	2.144E-02	8.532E-01	3.558E+00	1.139E-03	6.812E-01	6.744E-02
800x800	6.739E-02	2.727E-01	4.171E-01	1.296E-02	7.264E-01	1.664E+00	8.198E-04	4.742E-01	1.952E-02

The right column of Figure 25 displays the relative error in the density for the same uniform grids as in the left column. The same features pointed out in density plots in the left column are apparent here, but it is also clear that the accuracy of the simulation dramatically improves as the resolution is increased. Not only does the shock thickness decrease, but the overall amplitude of the variations within the shocked region decreases as well. Table 9 demonstrates the global L_1 error norm decreases as the spatial resolution increases, but the rate decreases as the resolution is increased. In addition, the images aren't symmetric at any spatial resolution, suggesting the underlying numerical solution isn't axisymmetric. In addition, the relative error in the density is larger for locations near the z-axis than for points near the r-axis.

In the left column of Figure 26 is the numerical solution for the pressure on uniform grids of 100x100, 200x200, 400x400, and 800x800 at the final time of t=0.3 s. There is none of the striping, valleys, and herringbone features that are so prominent in the density fields. This demonstrates the importance of analyzing more than a single field for a given problem. However, there is a distinct sharpening of the shock interface as the spatial resolution is increased.
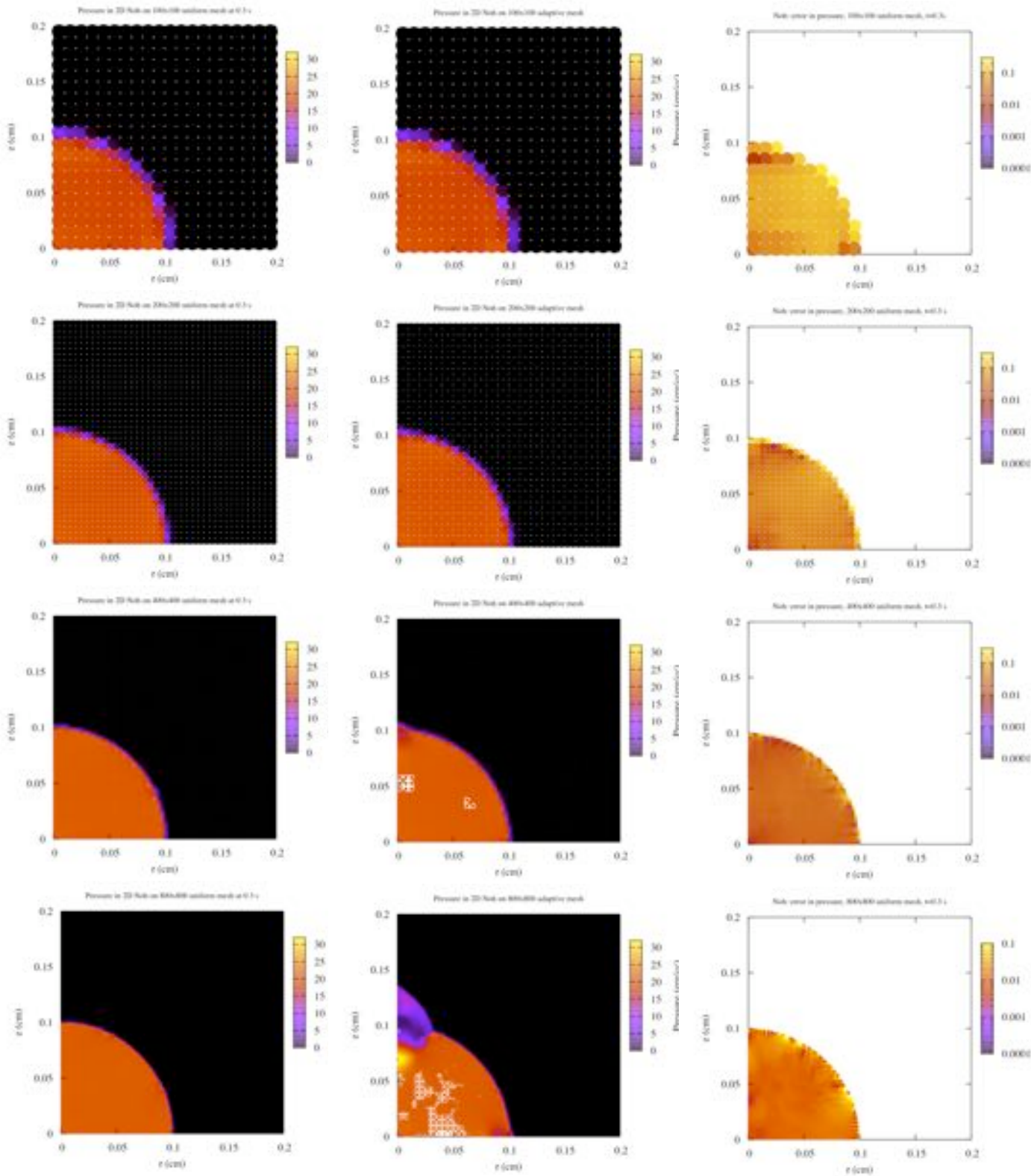
Figure 26. - Pressure field on uniform grids (left), pressure field on adaptive grids (middle) and relative error in the pressure on uniform grids (right) for the Noh problem. The spatial resolution is 100x100, 200x200, 400x400, and 800x800 grids (top to bottom) at t=0.3 s

The middle column of Figure 26 is the adaptive mesh analogue of the left column. Like the density fields, a low pressure bubble straddling the shock becomes obvious as the resolution is increased. The white areas between the origin and shock front at the 400x400 and 800x800 resolutions are regions that have de-refined (no dots to plot). The right column of Figure 26 displays the relative error in the pressure for the same uniform grids. For these images, white areas indicate an error of zero, that is, the numerical and analytical solutions agree exactly in the upstream material There are some grid-aligned structures near the shock front, but they are much less pronounced than they are for the density field. Table 9 establishes that the convergence rate for the pressure field is slightly sub-linear and decreasing as the spatial resolution is increased.

Asymmetries in the numerical solutions to the Noh problem are illustrated in Figure 27. Across any row is the asymmetry in the mass density, and pressure. Down any column are the asymmetries on 100x100, 200x200, 400x400, and 800x800 uniform grids at the ending time t=0.3 s. As in previous sections, the color maps plot the relative difference between the field at a given radius ($\sqrt{r^2 + z^2}$) and its radially-averaged value, yielding images of the deviations from spherical symmetry. Both the density and pressure fields have a rough axis of symmetry about the diagonal and have their largest deviations from spherical symmetry near the coordinate axes.
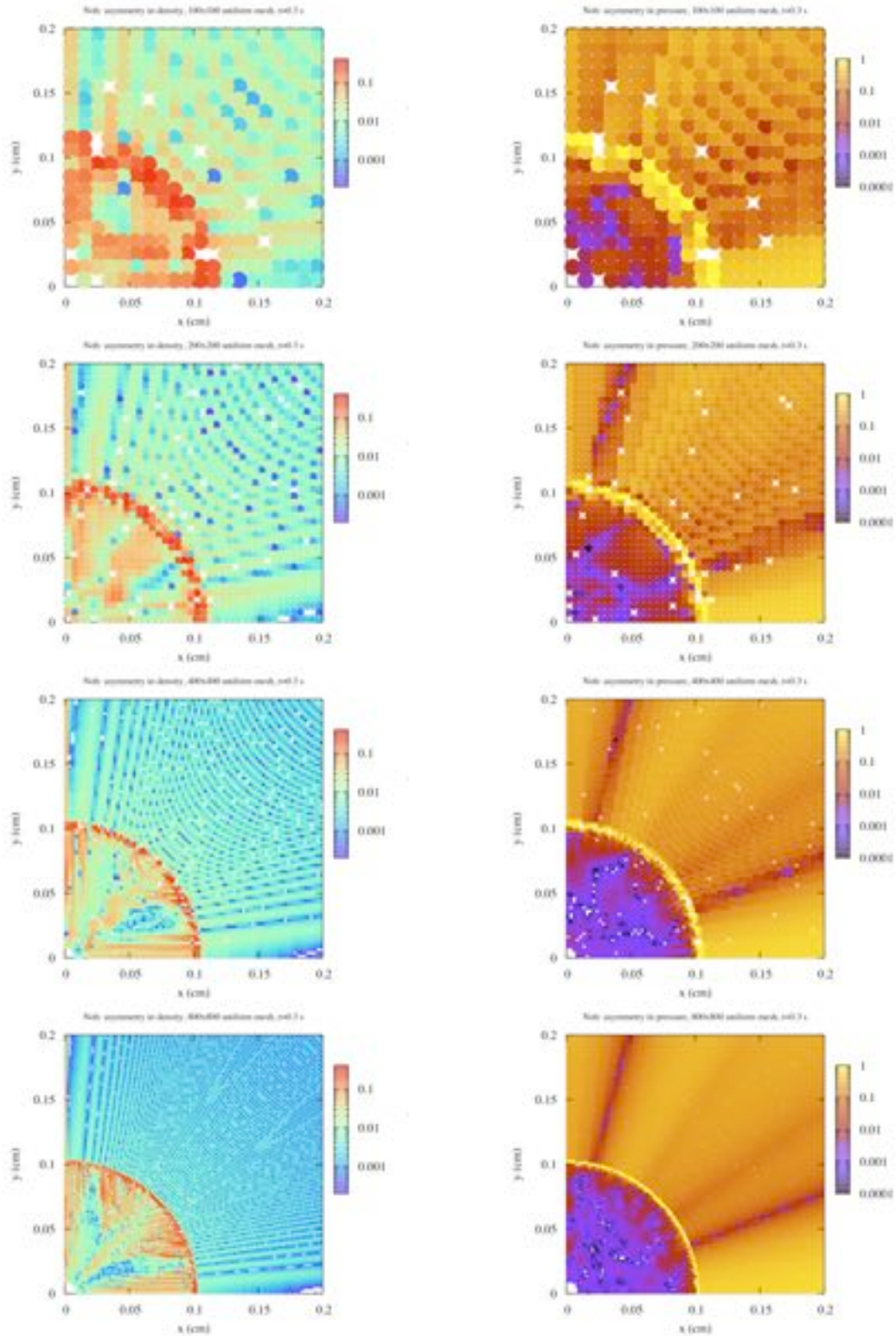
Figure 27. - Asymmetries in the numerical solutions of the Noh problem for the density (left) and pressure (right) on 100x100, 200x200, 400x400, and 800x800 uniform grids at t=1.0.

2.6 The Sedov Problem

A finite amount of energy is released at the origin at an initial time. The problem of finding self-similar, one-dimensional solutions for compressible hydrodynamics was considered by Sedov (1959), Taylor (1950), and von Neumann (1947). Sedov provided the most general closed-form solution, which we employ in the forms considered by Kamm (2000b). A description of the solution to the Sedov problem, including regularization of the singularities at the lower limits of integration and fortran code for generating solutions, is given by Timmes, Gisler & Hrbek (2005) and the spatial-temporal convergence properties are discussed in Timmes, Fryxell & Hrbek (2006).
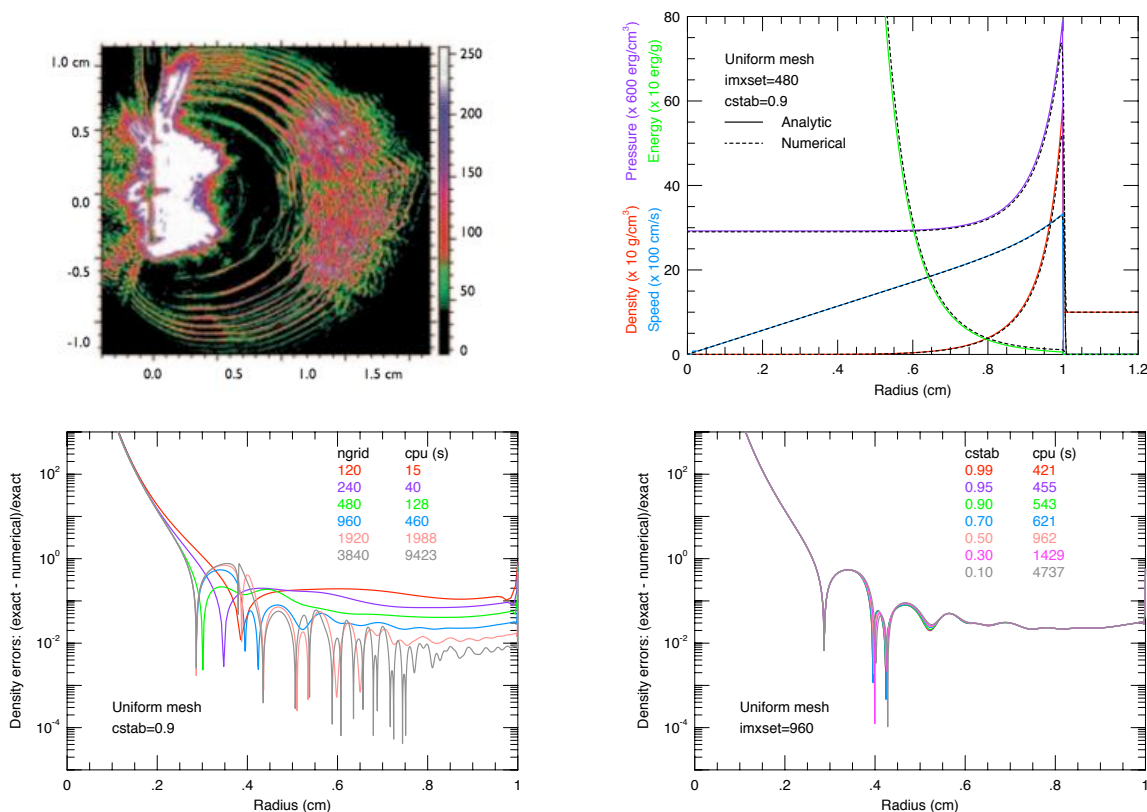

Figure 28. - Summary of the Sedov problem in 1D. Shown are a multiple-frame shadowgraph from the Trident laser studying the stability of a Taylor-Sedov blast wave (upper left), numerical and analytical solutions (upper right), relative errors in the density for a variety of uniform grids at a fixed time-step control value (lower left), and the relative error in the density for a variety of time-step control values on a fixed uniform grids.

Figure 28 displays a representative solution on a 480 cell uniform mesh with a time-step controller of cstab=0.9 in the upper right at the final time of t=1.0 s. The parameter cstab sets the time-step based on the local sound speed and the material velocity, $\Delta t = \text{cstab} \cdot \Delta x / (c + \max(|v_x| + |v_y| + |v_z|))$, and determines the time-step in the numerical solution of the Sedov problem. Initialization of the Sedov problem will generate a spirited discussion whose antagonists are divided between depositing all the energy into a single central zone or depositing the energy

in a small fixed size region. While the one-cell case is perhaps a more authentic way of initializing the problem, it is rarely seen in the refereed literature. (Reile & Gehren 1991; Buchler et al 1997; Fryxell et al. 2000; although see Swesty & Myra 2006). For the 2D results dicussed in this report, the fixed size region initialization was used. Results for both initialization procedures on 1D grids are discussed in Timmes, Fryxell, & Hrbek (2006). Analytical and numerical solutions are overlayed for the mass density, pressure, specific internal energy, and material speed. The analytic and numerical solutions generally agree at a visual level of comparison except near the origin.

The image in the lower left of Figure 28 displays the absolute value of the relative errors in the density for a variety of uniform grids at the final time of 1.0 s. The relative cpu cost on a single processor of increasing the spatial resolution is given. The singularity at the origin means $T(r \rightarrow 0) \rightarrow \infty$, implying large errors in the specific energy. For radii $\gtrsim$ 0.4 cm, there is a steady decline in the magnitude of the errors between the origin and the shock front as the spatial resolution is increased. Figure 28 suggests that for $r \gtrsim$ 0.4 cm, the density (and other quantities) have roughly linear convergence rates ($\alpha \sim 1$). Including the $r \lesssim$ 0.4 cm region leads to smaller convergence rates because of the persistent errors at the origin. For the fixed region initialization procedure we find, in 1D, the same convergence rates to within 2 significant figures (Timmes, Fryxell, & Hrbek 2006).

The image in the lower right of Figure 28 exhibits the absolute value of the relative errors in the density for a variety of time-step control values on a uniform grid of 960 cells. The relative cpu cost on a single processor of increasing the temporal resolution is shown. Figure 28 implies that the density (and other quantities) have a convergence rate near zero, which suggests that the spatial discretization may dominate the error budget.

In the left column of Figure 29 is the numerical solution for the density on uniform grids of 120x120, 240x240, 480x480, and 960x960 at the final time of t=1.0 s. As the spatial resolution is increased, the shock front becomes thinner and better defined. In the viewgraph norm, RAGE appears to do well on the density field despite the asymmetrical, instability-looking material for radii less than 0.4 cm. This material has a density that is 4 to 5 orders-of-magnitude smaller than the upstream density and probably doesn't effect the blast wave at a radii of 1.0 cm. The asymmetries in the density field of 2D Sedov problem are considerably less concerning than in the density field of the 2D Noh problem. This is a natural consequence of the kinematics: expansions smooth out asymmetries while compressions exacerbate them. A careful examination of the density field reveals that the shock front has (correctly) reached 1.0 cm along the r-axis, but the position of the shock is slightly less than 1.0 cm along the z-axis. That is, the shock front is asymmetrical.

The middle column of Figure 29 is the adaptive mesh analogue of the left column. Dots in the figure represent the grid pints where the various solutions were computed, the color of the dot indicative of the magnitude of the density field. White areas indicate regions where there is no grid (i.e., de-refinement has occurred), while regions of heavy refinement yield solid color maps. The base grid from which refinement began is a uniform 120x120 mesh. The maximum spatial resolution of each adaptive mesh is equal to its uniform mesh counterpart. In the 2D Sedov problem, the adaptive grid refinement works very well, concentrating the computing burden where it is most needed, at the shock, and in saving considerable computational expense. The adaptive mesh runs for the density field of 2D Sedov problem don't show hints of the disastrous anomaly that bedevils the density fields in the adaptive runs for the 2D Noh problem. In addition, most of the fine detail in the Rayleigh-Taylor unstable material is largely absent in the adaptive mesh runs. However, like the uniform grid case, the position of the shock along the z-axis is slightly smaller

than the location of the shock along the r-axis.

The right column of Figure 29 displays the relative error in the density for the same uniform grids as in the left column. The relative errors are large for radii less that 0.4 cm due to the turbulent-like flows in this region and are largely independent of spatial resolution. For radii larger than 0.4 cm, the errors are small and become smaller as the spatial resolution is increased. The cusps, indicative of a change in sign in the relative error, are asymmetrical indicating that the 2D numerical solution on uniform grids is generating some asymmetries. Note that the errors at the shock front for locations near the z-axis are larger than the relative errors for locations near the r-axis. This is another indication that the shock along the z-axis lags the shock along the r-axis.

Table 10 details the convergence properties for the 2D Sedov problem on uniform grids, and Table 11 does the same for adaptive grids. These tables indicate the density has a convergence rate $\alpha \sim 0.5$ that appears to be decreasing as the spatial resolution increases. It is encouraging that the convergence indices are roughly the same for both uniform and adaptive grids.

Table 10
Spatial Convergence Coefficients for the Sedov Problem on 2D Uniform Grids

# of cells	Density $L_{1,abs}$	α	A	Pressure $L_{1,abs}$	α	A
120x120	9.812E-02			2.137E-03		
240x240	6.263E-02	6.478E-01	1.938E+00	1.376E-03	6.350E-01	3.981E-02
480x480	3.848E-02	7.027E-01	2.592E+00	8.385E-04	7.149E-01	6.079E-02
960x960	2.627E-02	5.506E-01	1.042E+00	5.614E-04	5.789E-01	2.690E-02

# of cells	Internal Energy $L_{1,abs}$	α	A	Speed $L_{1,abs}$	α	A
120x120	1.403E-01			6.220E-03		
240x240	1.021E-01	4.591E-01	1.162E+00	3.750E-03	7.302E-01	1.795E-01
480x480	8.591E-02	2.486E-01	3.811E-01	2.435E-03	6.230E-01	1.017E-01
960x960	9.411E-02	-1.315E-01	3.908E-02	2.041E-03	2.546E-01	1.119E-02

Table 11
Spatial Convergence Coefficients for the Sedov Problem on 2D Adaptive Grids

maximum # of cells	total # of cells	Density $L_{1,abs}$	α	A	Pressure $L_{1,abs}$	α	A
120x120	14400	9.812E-02			2.137E-03		
240x240	22940	9.996E-02	-2.671E-02	8.677E-02	2.143E-03	-3.897E-03	2.099E-03
480x480	31996	7.558E-02	4.034E-01	8.473E-01	1.657E-03	3.714E-01	1.533E-02
960x960	52380	5.921E-02	3.521E-01	6.232E-01	1.386E-03	2.576E-01	7.755E-03

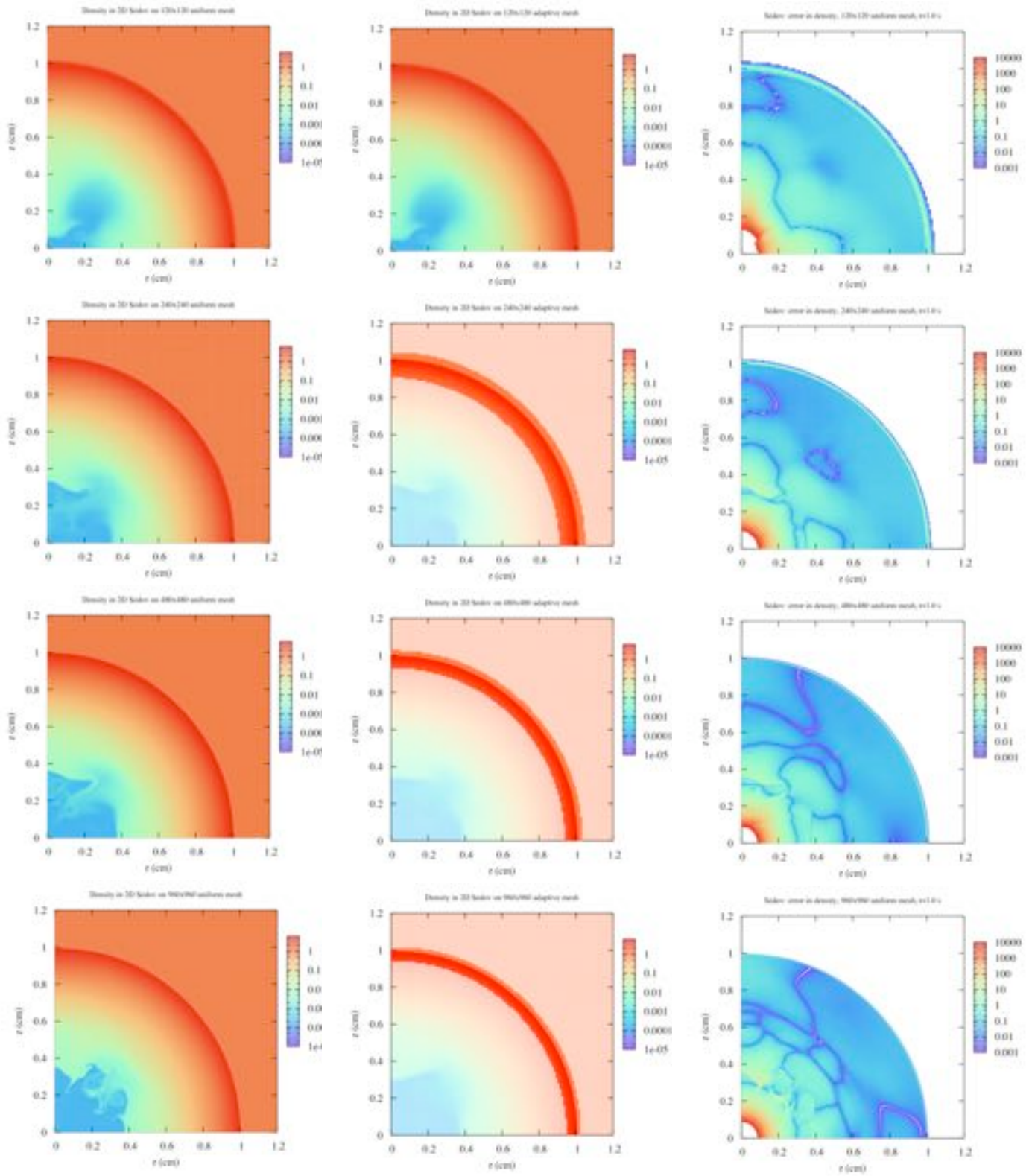| maximum # of cells	total	Internal Energy $L_{1,abs}$	α	A	Speed $L_{1,abs}$	α	A
120x120	14400	1.403E-01			6.220E-03		
240x240	22940	9.044E-02	6.336E-01	2.596E+00	5.901E-03	7.588E-02	8.822E-03
480x480	31996	7.359E-02	2.975E-01	4.375E-01	5.112E-03	2.073E-01	1.770E-02
960x960	52380	6.916E-02	8.943E-02	1.257E-01	4.596E-03	1.536E-01	1.283E-02

Figure 29. - Density field on uniform grids (left), density field on adaptive grids (middle) and relative error in the density on uniform grids (right) for the Sedov problem. The spatial resolution is 120x120, 240x240, 480x480, and 960x960 grids (top to bottom) at t=1.0 s

In the left column of Figure 30 is the numerical solution for the pressure on uniform grids of 120x120, 240x240, 480x480, and 960x960 at the final time of t=1.0 s. In the pressure field, there are none of the fluid instabilities signatures that are so prominent in the density fields. However, the fact the shock along the z-axis hasn't reached the correct value of 1.0 cm is more readily visible in the pressure field. The middle column of Figure 30 is the adaptive mesh analogue of the left column. The images demonstrate that as the spatial resolution is increased the pressure along the z-axis becomes larger (more white) that the pressure along the r axis. In fact, at the highest spatial resolutions the pressure along the shock front is asymmetrical. The right column of Figure 30 displays the relative error (compared to the analytic solution) in the pressure for uniform grids. The anomalous strengthening of the pressure for locations near the z-axis is evident. These are probably anomalous artifacts of RAGE's hydrodynamics.

Figure 31 gives the magnitude of the material velocity vector in the same format as for the density fields (Figure 29) and pressure field (Figure 30). The material speeds display the fluid instability features present in the density fields. Like the density and pressure fields, there are numerous asymmetrical cusps and the shock front fails to reach the correct position along the z-axis (darker shades in the relative error).

These difficulties in the Sedov test problem were only hinted at in last year's Tri-Lab Verification report (Timmes, Gisler & Hrbek 2005) because they only examined the density field. This demonstrates the importance of analyzing more than a single field for a given problem.

Asymmetries in the numerical solutions to the Sedov problem are illustrated in Figure 32 for uniform grids and in Figure 33 for adaptive grids. Across any row is the asymmetry in the mass density, pressure, and material speed. Down any column are the asymmetries on 120x120, 240x240, 480x480, and 960x960 uniform grids at the ending time t=1.0 s. As in previous sections, the color maps plot the relative difference between the field at a given radius ($\sqrt{r^2 + z^2}$) and its radially-averaged value. This yields one measure of the deviations from spherical symmetry. Note this is strictly a symmetry test of the numerical solution; the analytical solution doesn't enter the analysis. All the fields show the shock not reaching the correct location along the z-axis by having a larger deviation from the radially-average value.
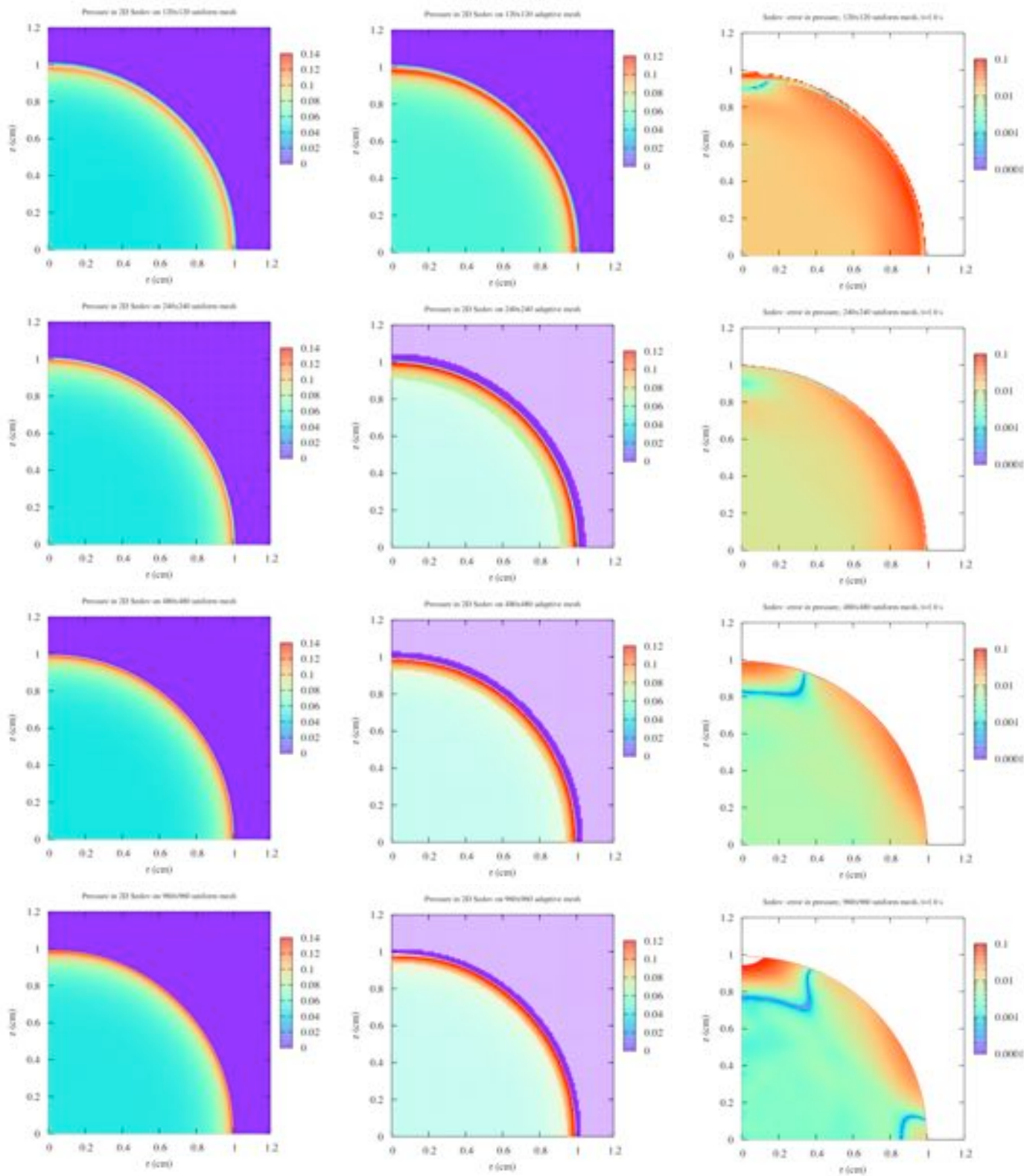
Figure 30. - Pressure field on uniform grids (left), pressure field on adaptive grids (middle) and relative error in the pressure on uniform grids (right) for the Sedov problem. The spatial resolution is 120x120, 240x240, 480x480, and 960x960 grids (top to bottom) at t=1.0 s
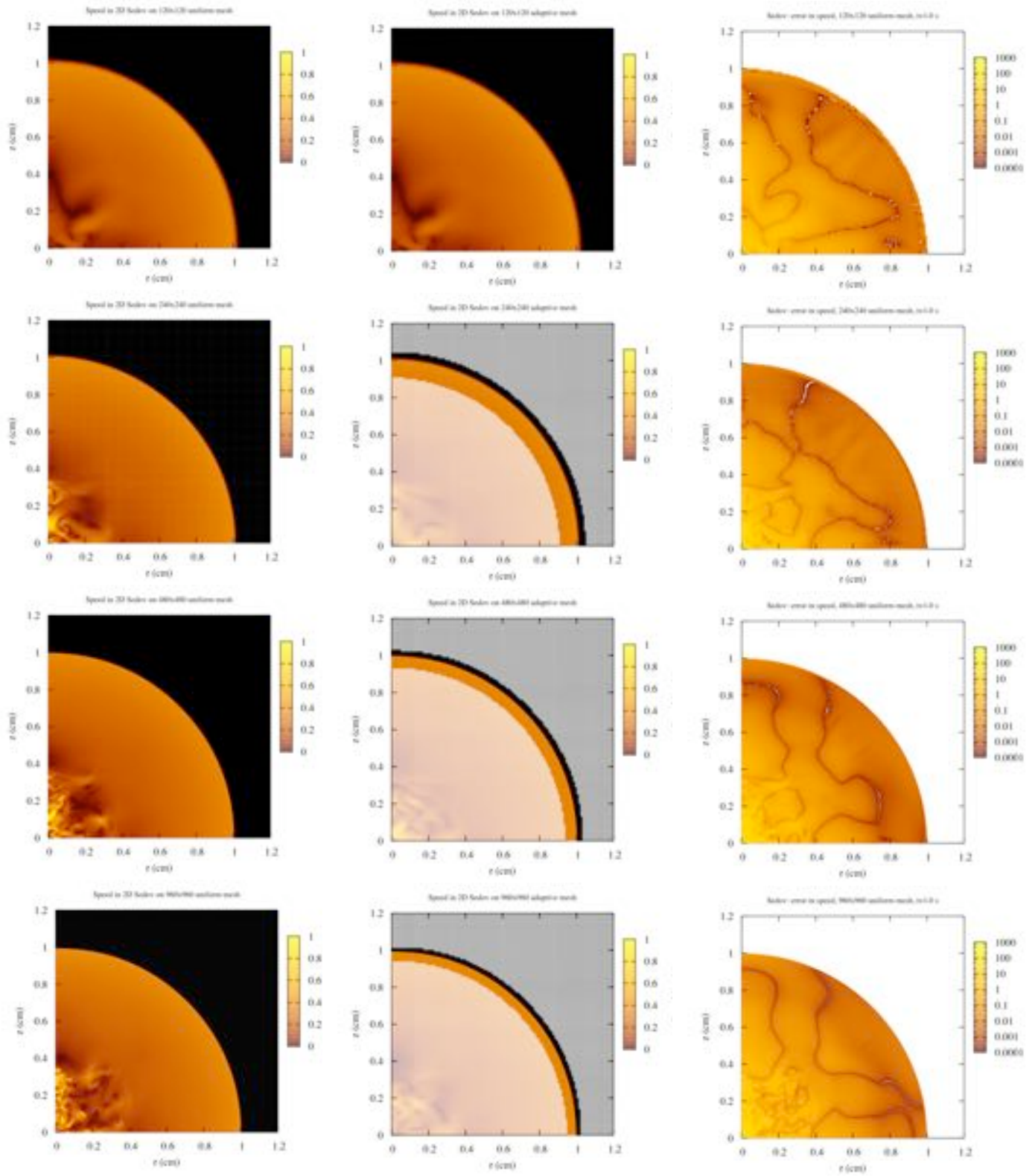
Figure 31. - Material speed on uniform grids (left), material speed on adaptive grids (middle) and relative error in the material speed on uniform grids (right) for the Sedov problem. The spatial resolution is 120x120, 240x240, 480x480, and 960x960 grids (top to bottom) at t=1.0 s
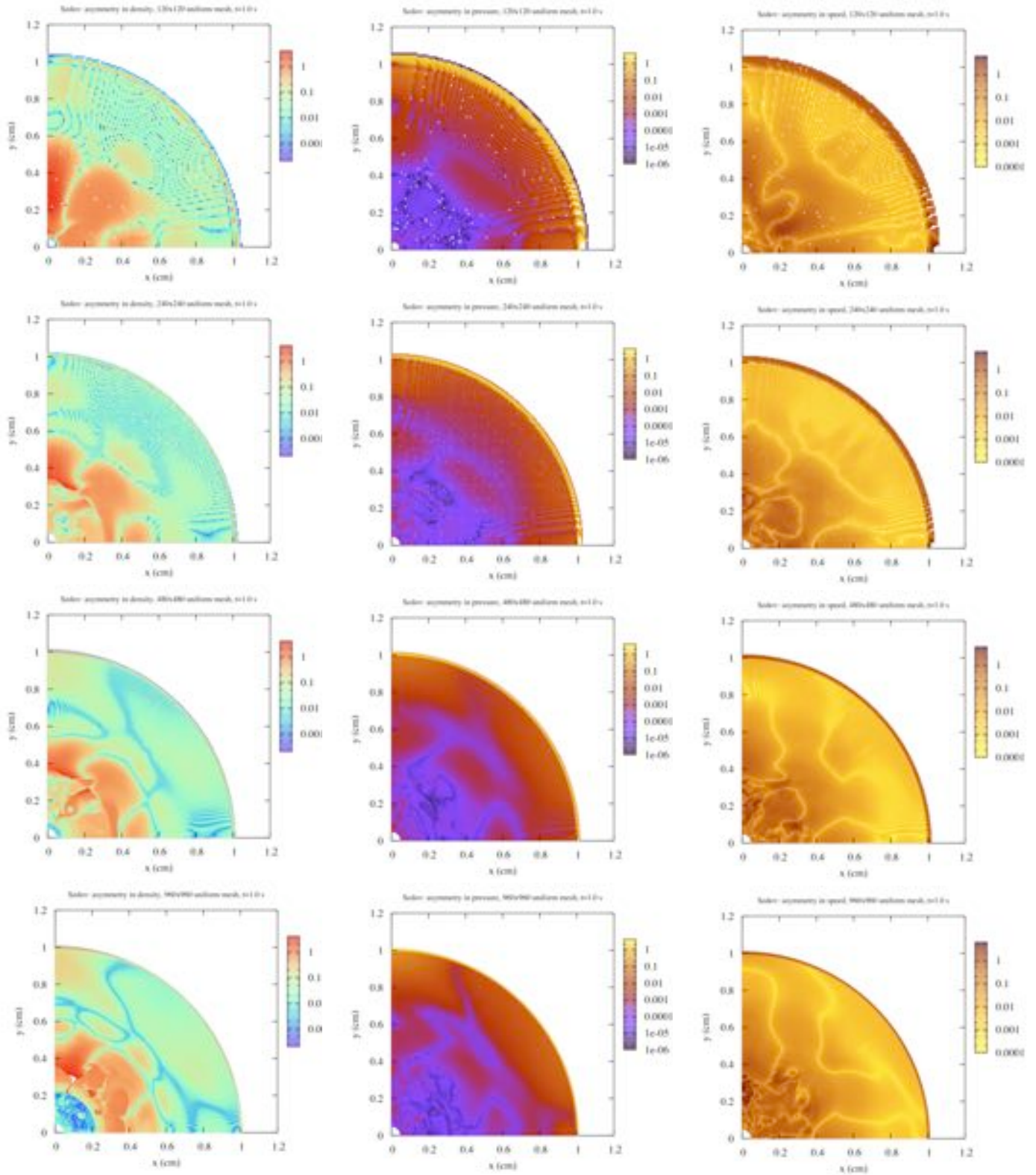
Figure 32. - *Asymmetries in the numerical solution of the Sedov problem for the density (left), pressure (middle), and material speed (right) on 120x120, 240x240, 480x480, and 960x960 uniform grids (top to bottom) at t=1.0 s.*
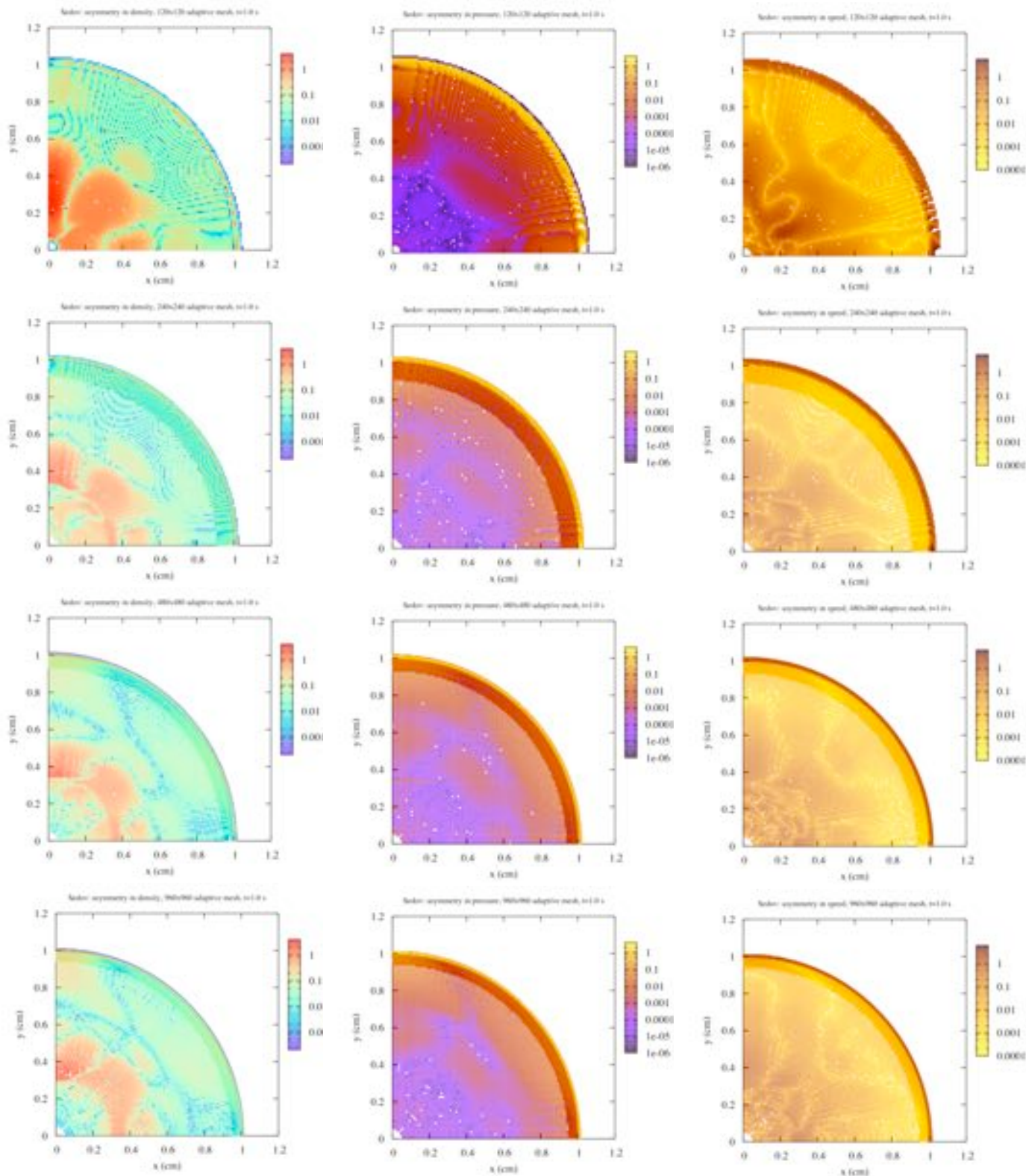
Figure 33. - Asymmetries in the numerical solution of the Sedov problem for the density (left), pressure (middle), and material speed (right) on adaptive grids with potential maximum resolutions of 120x120, 240x240, 480x480, and 960x960 (top to bottom) at t=1.0 s.

3. Conclusions and Future Directions

This report has described a verification analysis on uniform and adaptive meshes for multi-dimensional versions of the problems in the Tri-Lab Verification Test Suite. Previous efforts along these lines considered only the Noh and Sedov test problems in 2D on uniform (Kamm & Kirkpatrick 2004) and adaptive (Timmes, Gisler & Hrbek 2005) meshes. In general, RAGE shows a high degree of symmetry and fidelity to the underlying physics for test problems in slab geometries. All of the test problems run in axisymmetric geometries have problems with either large asymmetries or outright anomalies, particularly for locations near the z-axis. The Cog-8 problem has large errors for locations near the z-axis, the RMTV problem shows larger errors on adaptive grids than on the corresponding uniform grids, the Noh problem has a disastrous low density bubble near the z-axis on adaptive meshes, and the shock fails to reach the correct location along the z-axis for the Sedov problem because of a high pressure bubble.

The computational efficiency gained by using adaptive grids instead of uniform grids is typically about a factor of twenty for 4-6 levels of mesh refinement for most 2D versions of the problems in the Tri-Lab Verifications Test Suite. This efficiency gain, however, isn't generally accompanied by a corresponding reduction in the global error norm between the numerical and analytical solutions when the default AMR settings are used. For several Tri-Lab test problems (e.g., RMTV) the relative errors on adaptive grids are larger than the errors on corresponding uniform grids.

The efforts that led to this report spawned a new project to perform a daily execution of an automated spatial-temporal verification analysis for 2D versions of the Tri-Lab Verification Test Suite. Generating numerical solutions, comparing the numerical and analytical solutions, performing the verification analysis, and plotting the key results has become part of Code Project A's nightly regression testing. In addition to being incorporated into the daily regression tests, all the analytic solution codes, input decks, and `gold' results are now archived on SourceForge.

During the coarse of these investigations a new initialization module for the Reinicke Meyer-ter-Vehn problem was developed in tandem with Mike Clover (SAIC). This new module permits running the RMTV test problem in 2D and 3D for the first time. The new module also provides an accurate and smooth initial state, which is of particular importance for convergence studies on adaptive meshes. A new analytic solution for the two-dimensional cell-averaged solution of the Coggeshall #8 problem (Timmes & Clover 2006) was discovered. The new solution reduces the global error norm and smooths the error fields. This new solution is implemented in RAGE. In addition, Livermore's efforts to deploy the Tri-Lab Verification Test Suite on their codes include the use of four of our analytic solution codes (Su & Olson, Cog8, RMTV, and Mader).

New test problems that exercise multi-material and/or multi-temperature solutions in an extension of the Tri-Lab Verification Test Suite are needed and will be discussed with Livermore and Sandia at NECDC|06. As new analytic test problems are added to the Tri-Lab Test Suite, conducting the verification analysis on multi-dimensional versions of the test problems must be encouraged. In parallel, calculation verification procedures for complex physics problems that admit no exact solution must be encouraged to advance. The standard approach to conducting verification analysis where no exact solution exists presents two significant limitations. First, computational solutions that converge by oscillation are not calculable, and second, the technique is limited to a simple error model. An improvement to the current method is needed. Calculation verification offers a rigorous procedure for complex physics problems that don't admit an exact solution (Smitherman, Kamm & Brock 2005; Tippett & Timmes 2006). In calculation verification, the

absolute value of the pointwise error is calculated, allowing for local oscillatory convergence. The equations are then solved using Newton's method for the convergence constants, discretization errors, and an estimated exact solution simultaneously. This procedure allows for a more complex error model if desired.

Questions of analytic test problem relevance to realistic applications can be addressed by (1) creating new metrics from the existing Tri-Lab Test Suite, (2) constructing new analytic test problems that exercise multi-material and/or multi-temperature solutions, (3) developing calculation verification into a robust tool capable of performing well on complicated, multi-physics problems, and (4) integrating analyses of the numerical errors from spatial and temporal discretizations into quantification of margins and uncertainty (QMU) studies.

4. Acknowledgments

5. References

Brock, J., Isolating Temporal-Discretization Errors for Separate-Verification Analysis, AIAA Aerospace Sciences Conference, January 2004, AIAA-2004-0741, LA-UR-03-9160.

Buchler, J.R., Kollath, Z., & Marom, A., ``An Adaptive Code for Radial Stellar Model Pulsations'' , Astrophys. Space Sci. 253, 139, 1997.

Clover, M., Kamm, J.R., & Rider, W.J., ``An Example of Verification Analysis for an Eulerian Hydrocode'', LA-UR-00-5371.

Clover, M., ``Analytic Test Problem Setups in Crestone'', in preparation, 2006.

Coggeshall, S.V., Phys. Fluids A, 3, 5, 1991.

Fickett, W., and Davis, W.C., Detonation, (UC Berkeley, 1979).

Fryxell, B., Olson, K.,Ricker, P., Timmes, F.X., Zingale, M., Lamb, D.A., MacNeice, P., Rosner, R., Truran, J.W., & Tufo, K., ``FLASH: An Adaptive Mesh Hydrodynamics Code for Modeling Astrophysical Thermonuclear Flashes'', Astrophys. J. Suppl. 131, 273, 2000.

Grove, J., AMHCTOOLS, LA-CC-05-052, 2005a.

Grove, J., AMHCTOOLS, LA-UR-05-7425, 2005b.

Hemez, F.M., ``Non-linear Error Ansatz Models for Solution Verification in Computational Physics'' LA-UR-05-8228., 2005.

Hrbek, G.M., Timmes, F.X., Brock, J.S., Kamm, J.R., ``The Pinocchio Project: An Automated Scripting Tool For Performing Verification Analysis On Physical Simulation Codes Phase 1 Report'', LA-UR-05-3471, 2005.

Kamm, J.R., ``Investigation of the Reinicke & Meyer-ter-Vehn Equations: I. The Strong Conduction Case'', LA-UR-00-4304, 2000a.

Kamm, J.R., ``Evaluation of the Sedov-von Neumann-Taylor Blast Wave Solution'', LA-UR-00-6055, 2000b.

Kamm, J.R., Rider, W.J., Brock, J.S., ``Consistent Metrics For Code Verification'' LA-UR-02-6055, 2002.

Kamm, J.R., and Kirkpatrick, R., Verification analyses of code project A, LA-CP 04-04361, 2004.

Kirkpatrick, R., Wingate, C., Kamm, J., HE Burn Test Problem, X-3-19U, 2004.

Mader, C., Numerical Modeling of Explosives and Propellants, Second Edition CRC Press, Florida, 1997.

Noh, W.F., ``Errors for calculations of strong shocks using an artificial viscosity and an artificial heat flux'', J. Comp. Phys. 72, 78-120, 1987.

Reile, C., & Gehren, T., ``Numerical simulation of photospheric convection in solar-type stars I. Hydrodynamical test calculations'', Astron. Astrophys. 242, 142, 1991.

Reinicke, P., Meyer-ter-Vehn, J., ``The point explosion with heat conduction'', Phys. Fluids A, 1807, 3, 1991.

Rider, W.J., ``Revisiting Wall Heating'', J. Comp. Phys., 162, 395, 2000.

Smitherman, D.P., Kamm, J.R., Brock, J.S., ``Calculation Verification: Pointwise Estimation of Solutions and Their Method-associated Numerical Error'', LA-UR-05-8002, 2005.

Sedov, L.I., ``Similarity and Dimensional Methods in Mechanics'', Academic Press, New York, 1959.

Swesty, F.D., & Myra, E.S., ``A Numerical Algorithm for Modeling Multigroup Neutrino-Radiation Hydrodynamics in Two Spatial Dimensions'', Astrophys. J., submitted, 2006.

Su, B., and Olson, G.L., J. Quant. Spectro. Radiat. Transfer, 56, 3, 1996.

Taylor, G.I., ``The formation of a blast wave by a very intense explosion'', Proc. Roy. Soc. London A 201, 159, 1950.

Timmes, F.X., Clover, M., On a Cell-Averaged Solution to the Coggeshall #8 Problem, in preparation, 2006.

Timmes, F.X., Gisler, G., Hrbek, G.M., Automated Analyses of the Tri-Lab Verification Test Suite on Uniform and Adaptive Grids for Code Project A, LA-UR-05-6865, 2005.

Timmes, F.X., Fryxell, B., Hrbek, G.M., ``Spatial and temporal convergence properties of the Tri-Lab Verification Test suite for code project A'', LA-UR-06-6444, 2006.

Tippett, T., Timmes, F.X., Calculation Verification for Code Project A, in preparation, 2006.

Williams, T., et al., gnuplot 4.0 Users Manual, 2004